Master's thesis

NTNU
Norwegian University of Science and Technology
Faculty of Natural Sciences
Department of Chemical Engineering

Andrea Kjønli

Gas dechlorination of plastic pyrolysis derived oil with model compounds using Fe based material.

Master's thesis in Chemical Engineering and Biotechnology
Supervisor: Prof. De Chen
Co-supervisor: Dr. Ainara Moral Larrasoana
June 2023

NTNU
Norwegian University of
Science and Technology

Andrea Kjønli

Gas dechlorination of plastic pyrolysis derived oil with model compounds using Fe based material.

Master's thesis in Chemical Engineering and Biotechnology
Supervisor: Prof. De Chen
Co-supervisor: Dr. Ainara Moral Larrasoana
June 2023

Norwegian University of Science and Technology
Faculty of Natural Sciences
Department of Chemical Engineering

NTNU
Norwegian University of
Science and Technology

ABSTRACT

World plastic production has increased rapidly since the 1950s due to its excellent properties. Unfortunately, only a small fraction of this plastic is recycled, leading to massive amounts of plastic waste polluting our oceans and nature. This has resulted in harmful effects on the environment. Mechanical recycling is currently the most common method for plastic recycling. Unfortunately, mechanical recycling has its limitations due to difficulties in the removal of contaminations and produces lower-quality plastics. Pyrolysis has recently gained a lot of attention for plastic recycling because it more effectively manages the contaminations. However, PVC contains a high amount of chlorine, which can lead to the formation of chlorogenic compounds and cause problems for the steam crackers. Dechlorination has been suggested as a potential upgrading technology to remove the chlorine content from plastic waste.

This project is part of a collaboration with Quantafuel and focuses on reducing the chlorine content in the oil. The levels of chlorine in the oil are higher than the allowed limit of 10 ppm for the steam cracker. To lower the chlorine content, a model system of dechlorination of chlorobenzene, with a Fe-based sorbent, such as red mud. Chlorobenzene is chosen due to its known complexity of dechlorination.

The preparation of red mud involved drying and calcination at 550°C. The red mud was subjected to reduction temperatures of 350° and 500°, and washed with HCl. The regeneration effect was also investigated with a regeneration temperature of 350°C and 500°C. A reference sorbent with Fe/SiO_2 was prepared as well. The different characterization techniques used for this study were N_2 adsorption-desorption analysis, XRF, XRD, TGA and TPR. Washing the red mud with HCl caused the BET surface area to increase to 41.9 m^2/g, while also reducing the sodium content by 97% and the calcium content by 54%. It was discovered that it is possible that other elements in red mud might be active. In addition to inhomogeneity, this could cause the observed challenges with reproducibility in red mud. Although washing with HCl was attempted, it did not seem to have any impact on the activity or regeneration. It is possible that this lack of effect is due to the other elements in red mud forming nonreducible species under the experimental conditions. Nevertheless, red mud had the ability to regenerate more efficiently compared to Fe/SiO_2, indicating that other elements in red mud could cause this. Reactivity was also observed after the regeneration of red mud. This indicates that red mud is an interesting candidate for further investigation as a sorbent, in addition to its high concentration of ferric oxide and low cost as a by-product.

SAMMENDRAG

Verdens produksjon av plast har økt raskt siden 1950-tallet på grunn av dens utmerkede egenskaper. Dessverre blir bare en liten fraksjon av denne plasten resirkulert, noe som fører til massive mengder plastavfall som forurenser hav og natur. Dette har medført skadelige effekter på miljøet. Mekanisk resirkulering er den mest vanlige metoden for plastresirkulering i dag, men dessverre har den sine begrensninger på grunn av vanskeligheter for å fjerne forurensninger og produserer plast av lavere kvalitet. Pyrolyse har nylig fått mye oppmerksomhet for plastgjenvinning, på grunn av at den håndterer forurensninger bedre. Men PVC inneholder en høy mengde klor, som kan føre til dannelse av klorogene forbindelser og forårsake problemer for dampkrakkerne. Avkloriering har blitt foreslått som en potensiell oppgraderingsteknologi for å fjerne klorinnholdet fra plastavfall.

Dette prosjektet er en del av et samarbeid med Quantafuel og fokuserer på å redusere klorinnholdet i oljen til den tillatte grensen på 10 ppm for dampkrakkeren. For å senke klorinnholdet, vil det bli brukt et modellsystem for avklorering av klorbensen, med en Fe-basert sorbent, som rødslam. Klorbensen er valgt på grunn av dens kjente kompleksitet i avklorering.

Preparasjon av rødslam involverte tørking og kalsinering ved 550°C. Rødslam ble utsatt for reduksjonstemperature på 350°C og 500°C, og vasket med HCl. Regenereringseffekten for rødslam ble også undersøkt med en regenereringstemperatur på 350°C og 500°C. Fe/SiO_2 ble prepart for å bruke som en referanse. De forskjellige karakteriseringsmetodene som ble brukt i denne studien var N_2 adsorpsjon-desorpsjon analyse, XRF, XRD, TGA og TPR. Vasking av rødslam med HCl førte til at BET-overflatearealet økte til 41.9 cm^2/g, samtidig som natriuminnholdet ble redusert med 97% og kalsiuminnholdet med 54%. Ved aktivitetstesting, ble det oppdaget at andre elementer i rødslam muligens kan være aktive. I tillegg til inhomogenitet kan dette føre til utfordringer med reproduksjonsevne i rødslam. Selv om vasking med HCl ble forsøkt, syntes det ikke å ha noen innvirkning på aktiviteten eller regenereringen. Det er mulig at dette skyldes de andre elementene i rødslam som danner faser som ikke kan bli redusert under disse eksperimentelle forholdene. Likevel hadde rødslam evnen til å regenerere mer effektivt sammenlignet med Fe/SiO_2, noe som indikerer at andre elementer i rødslam forårsake dette. Reaktivitet ble også observert etter regenereringen av rødslam. Dette indikerer at rødslam er en interessant kandidat for videre undersøkelser som en sorbent, i tillegg til sin høye konsentrasjon av jernoksid og lave kostnader som et biprodukt.

PREFACE

This master's thesis is written in collaboration with the Department of Chemical Engineering at NTNU. This thesis explores the potential of plastic pyrolysis as a solution to the growing problem of plastic waste, with a focus on eliminating contaminations like chlorine with a model system of dechlorination. The results of this research could have significant implications for the future of waste management in our society. I hope you find this thesis informative and thought-provoking.

For this thesis, I would like to express my gratitude and appreciation towards the many individuals in the catalysis group at the Department of Chemical Engineering at NTNU, who have made the research on gas dechlorination with a model system possible. In particular, I have to express thanks to Professor De Chen and Doctor Ainara Moral Larrasoana, whose experience, guidance and support have been invaluable throughout the entire research process.

CONTENTS

LIST OF FIGURES

LIST OF TABLES

ABBREVIATIONS

OECD	=	Co-operation and Development
PS	=	Polystyrene
PE	=	polyethylene
PVC	=	Polyvinyl chloride
HDPE	=	High density polyethylene
LDPE	=	Low density polyethyelene
PP	=	Polypropylene
PET	=	Polyethylene tetraphalate
SBR	=	Solvent-based recycling
HCl	=	Hydrochloric acid
TPR	=	Temperature programmed reduction
XRD	=	X-ray powder diffraction
XRF	=	X-ray Fluorescence
TGA	=	Thermogravimetric analysis
XAFS	=	X-ray adsorption fine structure spectroscopy
BET	=	Brunauer-Emmett-Teller
BJH	=	Barrett-Joyner-Halenda

CHAPTER

ONE

INTRODUCTION

Plastic is one of the most common basic materials in the world owing to its excellent durability, lightweight, low cost, and high machinability [1]. The different sectors of plastic are packaging, building and construction, automotive and electronics, with packaging being the largest among them. The exceptional properties of plastic have resulted in exponential growth in production, and as of 2015, 63000 million metric tons of plastic have been generated. Despite the numerous benefits of plastic, one significant issue associated with it is the huge amount of plastic ending up in landfills. As of 2015, 79% of the plastic ended up in landfills, 12% was incinerated and only 9% was recycled. The cumulative generation and disposal of plastic waste are depicted in figure 1.0.1. The solid lines illustrate historical data from 1950 to 2015 and the dashed lines illustrate projections of historical trends up to 2050 [2].

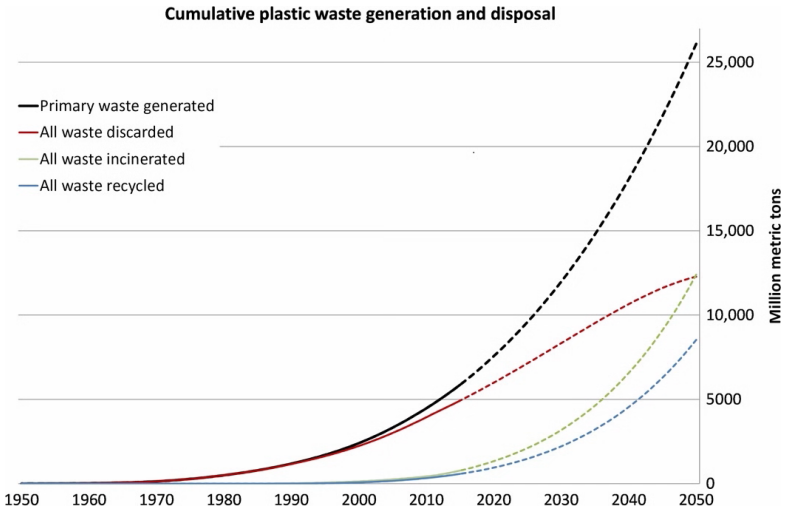

Figure 1.0.1: The cumulative plastic waste generation and disposal. The solid lines illustrate historical data from 1950 to 2015. The dashed lines illustrate projections of historical trends to 2050[2].

Based on the historical projections depicted in figure 1.0.1, it is expected that there will be a significant increase in the amount of waste generated and incinerated. While there will be an increase in recycled plastic, the growth will be at a lower rate. The majority of plastic currently follows a linear economy and is not recycled. A schematic illustration of plastic production, use, and disposal is illustrated in figure 1.0.2. The green path in figure 1.0.2 outlines the pathway of the circular economy, where plastic is collected for recycling.

Figure 1.0.2: A schematic illustration of plastic production and use. Taken from Buchnall D [3].

Single-use plastic is a major plastic leakage into the environment and counts for 30% of all plastics [4]. The considerable amount of plastic ending up in landfills and the natural environment is harmful and poses a significant threat to the environment. Plastic has a remarkably long lifespan and can take up to 1000 years to decompose naturally and pose problems for wildlife and their habitats. Additionally, plastic contains toxic dyes and additives [5] that can harm the environment. A more recent problem is microplastics, which are derived from larger pieces of plastic. These microplastics can enter the food chain and potentially harm humans and animals [6]. As much as 99% of all plastic is derived from a fossil feedstock, such as crude oil, hence plastic production could contribute to greenhouse gas emissions. In 2019, 1.8 billion tonnes of greenhouse gasses, with 90% of those emissions resulting from the conversion of fossil fuels into plastic[7].While plastic pollution is an issue that is on the rise, a complete ban on plastic is not a solution. The excellent properties of plastic contribute to a more sustainable society and a prohibition would cause greater harm to the environment. Because of the light weight of plastic, other materials such as metals and glass will double the energy consumption [1] during for example transportation and manufacturing. Plastic is incredibly useful in protecting food and reducing waste, as well as insulating elec-

trical cables for maximum efficiency[8]. The proposed solution to plastic pollution is to shift from a linear economy to a circular economy by increasing recycling efforts. This approach prevents plastic from ending up in the environment and decreases our dependency on fossil fuels. Recycling plastic also reduces CO_2 emissions by 30-80% [9].

In recent years, plastic policies have gained more attention to address the environmental problems with plastic waste. About 25.8 million tonnes of plastic waste is generated in Europe every year [10]. In response, the European Commission published the plastic strategy in 2018 [11], which aims to shift from a linear economy and improve plastic circularity. This strategy led to the banning of single-use plastic in the EU in July 2021. To implement the plastic strategy, the European Commission established a set of EU measures in 2018 [10]. The EU measure includes improving the economy and quality of plastic recycling, curbing plastic waste and littering and driving innovation and investments towards circular solutions.

In order to enhance the economics and quality of plastic recycling, the EU aims to increase the recycling of plastic packaging to 55% by 2025, and by 2030, all plastic packaging in the market should be easily recyclable and reusable. Additionally, the EU plans to establish quality standards for sorted plastic waste and recycled plastics to increase demand for recycled plastics. Furthermore, issuing new guidance for better and more harmonized separate collection and sorting can also improve the process. By 2025, the EU aims to transform 10 million tonnes of recycled plastics into new products for their market. EU aims to reduce the impact of plastic waste on our environment by implementing laws that restrict the production and usage of single-use plastics. Clear regulations with biodegradable properties are being established, along with lifecycle assessments to determine the conditions under which the use of biodegradable or compostable plastic is beneficial. Lastly, intentionally added microplastic will be restricted. The EU will promote circular solutions through innovation and investment. This involves enhancing sorting technologies, improving polymer design and exploring chemical recycling. Furthermore, the EU aims to produce materials that are completely biodegradable in both seawater and freshwater while remaining harmless to the environment and ecosystems. To minimize the environmental impact of plastic manufacturing, it is necessary to develop alternative feedstocks and internalize the environmental costs of landfilling and incineration by implementing high or gradually rising fees or taxes. Lastly, the EU will promote worldwide collaboration in waste management by supporting international initiatives, promoting best practices and utilizing external funding resources. The EU is dedicated to developing an innovative circular plastic industry globally, as well as encouraging international standards that increase industry confidence in the quality of recycled or recyclable plastics[10].

A global agreement on plastic waste was determined in March 2022 at the UN environment assembly in Nairobi. The goal is to complete a global legally binding agreement by the end of 2024 [12]. After the assembly, the Organization for Economic Co-operation and Development (OECD) projected global plastic scenarios

to 2060. A scenario without any policies, a baseline scenario, a regional action policy scenario, and a global ambition policy scenario were projected. Figure 1.0.3 show the scenario of plastic flow without policies.

.

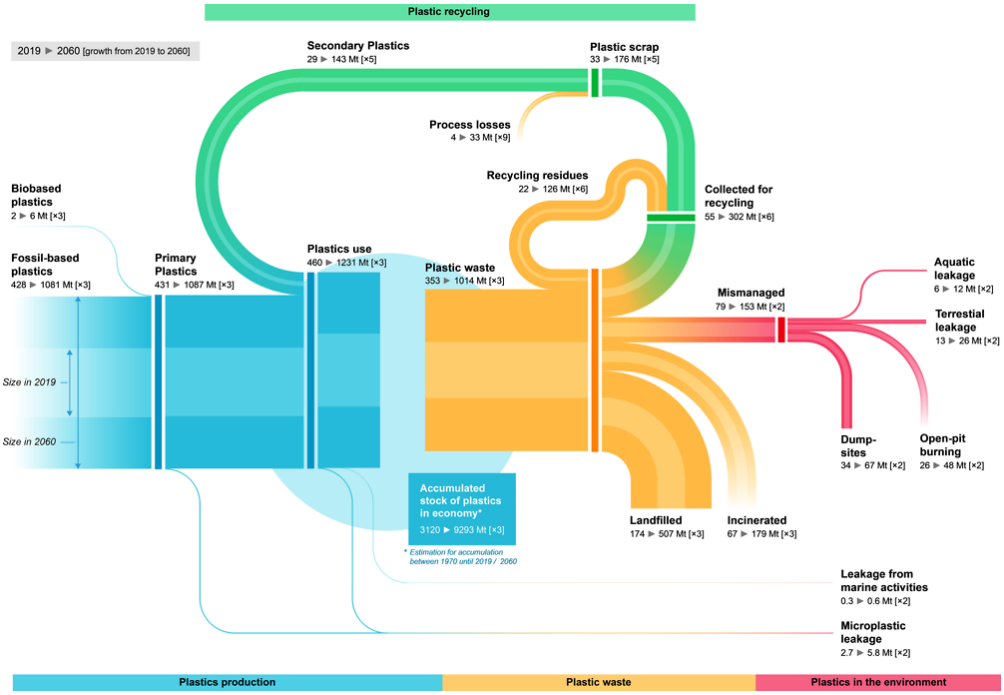

Figure 1.0.3: Plastic flow without policies [13]

Based on OECD's prediction in figure 1.0.3, the plastic lifecycle will only be 14% circular, and plastic waste will nearly triple, with half of it ending up in landfills by 2060. The amount of recycled plastic will only increase to 17%. Additionally, the greenhouse gas emissions are projected to increase from 1.8 Gt CO_2 in 2019 to 4.3 Gt CO_2e [13].

The Regional Action policy scenario aims to enhance plastic circularity and minimize its environmental impact. The Global Ambition policy share the same goal with Regional Action but sets a more challenging objective of achieving almost zero plastic leakage by 2060. According to the OECD, the Regional Action scenario predicts a 20% reduction in plastic waste compared to the baseline scenario, while the Global Ambition scenario predicts a 33% decrease [13]. These predictions are based on actions outline in table 1.0.1 and are compared to the baseline scenario.

Table 1.0.1: The actions in The Regional Action policy scenario and The global Ambition policy scenario [13]

Action	**The Regional Action policy scenario**	**The Global Ambition policy scenario**
Taxes on plastic	Increasing the tax to USD 750/tonne by 2060 and increase the taxes on packaging by one-third	Increasing taxes to USD 750/tonne by 2060 and to USD 1500/tonne by 2060 and increase the taxes on packaging by one-third
Global recycling rate	Increase to 40%	Increase to 60%
Secondary plastic surge	Increase from 12% to 29%	Increase to 41%
Mismanaged waste	Decline by more than 60%	Decline to net zero
Leakage to the environment		Falling to 85%
Reduce CO_2 emissions		By 2.1 Gt

Plastic is mainly produced from fossil fuels. Distillation of crude oil yields a gas fraction, liquid fraction and residues. The different distillation fractions from crude oil are shown in figure 1.0.4.

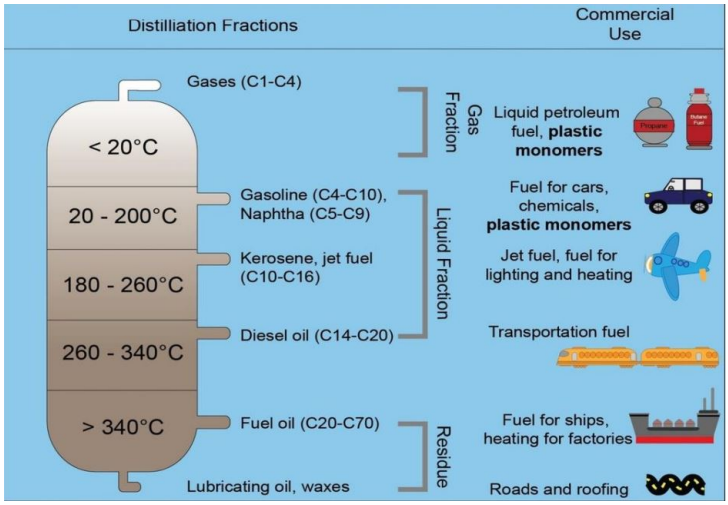

Figure 1.0.4: Distillation fraction and commercial use from crude oil [14].

As seen in figure 1.0.4, plastic monomers are produced from the liquid fraction naphtha (C_8-C_{12}) and the gas fraction. Plastic monomers are created through steam cracking of both naphtha and olefins by breaking down the hydrocarbons into smaller units. These monomers are then polymerized to produce various types of plastics [15]. 75% of the plastic is thermoplastic which can be melted and recycled, which does not soften when exposed to heat due to its strength and shape. This makes thermoset plastic unsuitable for single-use plastic and ideal for long-term use. The different types of thermoplastic polymers are polystyrene (PS), polyethylene (PE), polyvinyl chloride (PVC), and polyethylene (PE) which is divided into low and high density (HDPE & LDPE), polypropylene (PP) and polyethylene tetraphalate (PET). The majority of plastic is a combination of various polymers, with PE, PP and PET being the major polymers. Single-use plastic is made of PET, PE, and polyamide, and is lightweight, inexpensive, melt-processable, and processable. The major of the plastic is not recycled due to that recycling processes are expensive, resource-intensive and produces lower quality plastics [4].

It is four types of recycling processes, primary, secondary, tertiary, and quaternary recycling [16]. Figure 1.2.3 show the current plastic conversion technologies.

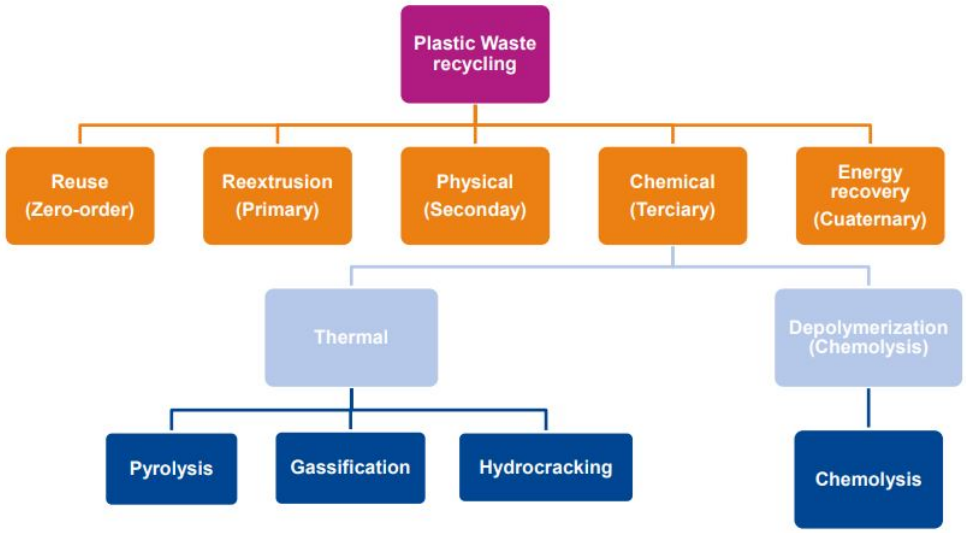

Figure 1.0.5: Current plastic conversion technologies. Taken from Ainara Moral Larrasoana.

Mechanical recycling is the most common recycling method today, which can be categorized into primary and secondary recycling. Primary recycling involves the mechanical recycling of virgin plastic, while secondary recycling involves the mechanical recycling of previously recycled plastic. Mechanical recycling involves different steps, such as separating and sorting, compacting/baling, washing, grinding, and compounding & pelletizing as seen in figure 1.0.6.
[17].

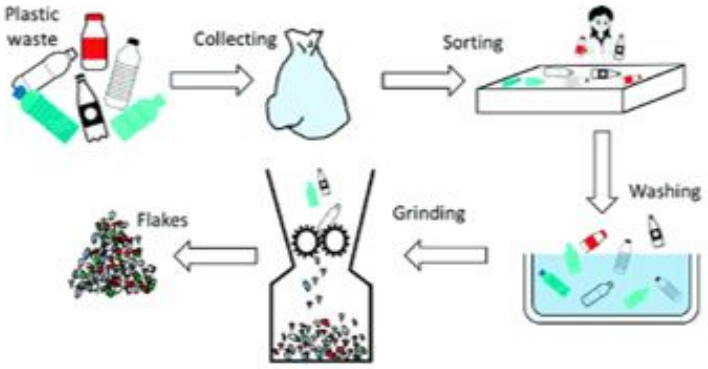

Figure 1.0.6: Different steps in mechanical recycling. Taken from Ragaert et al. 2017 [17]

Mechanical recycling produces lower-quality plastic and each cycle of secondary recycling will further decrease the quality [16]. Additionally, mechanical recycling is also laboring intensely due to the separating and sorting process which is necessary because the post-consumer plastic waste is mixed plastic. Furthermore, contaminations such as halogens, metals and additives pose a challenge to mechanical recycling[18]. Mechanical recycling is insufficient to handle the amount of recycled plastic due to these challenges. Therefore, upgrading recycling technologies is imperative for the creation of a more circular economy.

A promising solution to future plastic waste problems is chemical recycling, a tertiary recycling technology that can convert polymers into feedstock oil and potentially recycle plastic an infinite number of times. Chemical recycling has gained more attention in recent years and is a promising technology to handle future plastic waste problems. As seen in figure 1.2.3, chemical recycling is divided into thermolysis and chemolysis. Chemolysis breaks down polymers into monomers for plastic production through polymer chain scission, while thermolysis breaks polymer down with heat[19]. Chemical recycling includes technology such as pyrolysis, gasification, and depolymerization, and is more tolerant to complex waste streams and contaminations compared to mechanical recycling [20]. Quaternary recycling is energy recovery and can be used when the plastic waste is unsuitable for any other types of recycling [16]. Energy recovery is incineration and involves the release of CO_2, which necessitates the use of technologies to capture it which also requires a lot of energy. Therefore, this is not an ideal option for recycling.

Another promising technology to separate waste mixed plastics is the secondary mechanical recycling technology, solvent extraction [6]. Solvent extraction has the potential to be profitable and environmentally friendly, depending on the type of solvent used. Additionally, compared to mechanical recycling, solvent extraction can tolerate a higher level of contamination and complex waste streams [20]. The technology includes the dissolution/precipitation method and supercritical fluid extraction. During solvent extraction, the polymer is dissolved in the solvent, and the polymer is selectively crystallized and recovered.

Although chemical recycling has been considered a viable option, it still poses some challenges such as variations in waste composition, feedstock contamination, and the need for upgrading to ensure economic viability. Upgrading technologies are essential in optimizing the liquid yield and hydrocarbon production, especially naphthenes, which are used to create plastic. Furthermore, the process of chemical recycling, particularly pyrolysis, tends to be costlier as it requires a significant amount of energy and may have adverse effects on the environment. Compared to mechanical recycling, pyrolysis has a 7% higher impact on climate change, while it has a 50% lower impact when compared to energy recovery [21]. A desirable global plastic-waste generation scenario is simulated by McKinsley&Company [22]. The target is to increase the recycled plastic to 50% by 2030, by expansion of mechanical recycling and launching of two new technologies such as monomer recycling and pyrolysis. The model predicts that the amount of recycled plastic with pyrolysis increases from 0% to 13% as shown in figure 1.0.7.

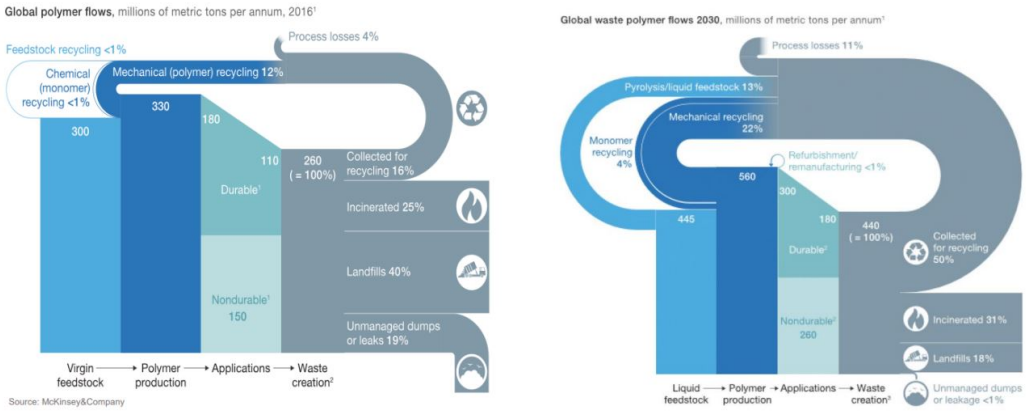

Figure 1.0.7: Global polymer flow per 2016 and a simulated model per 2030 by McKinsley&Company [22]

Even the model in figure 1.0.7 predicts an increase in recycling from 16% to 50%, this scenario will not be an option without technology to capture CO_2 from the incineration.

A recommended solution for recycling plastic waste is to combine the benefits of both chemical and mechanical recycling, as depicted in figure 1.0.8. The rejected plastic waste from mechanical recycling can be recycled through pyrolysis.

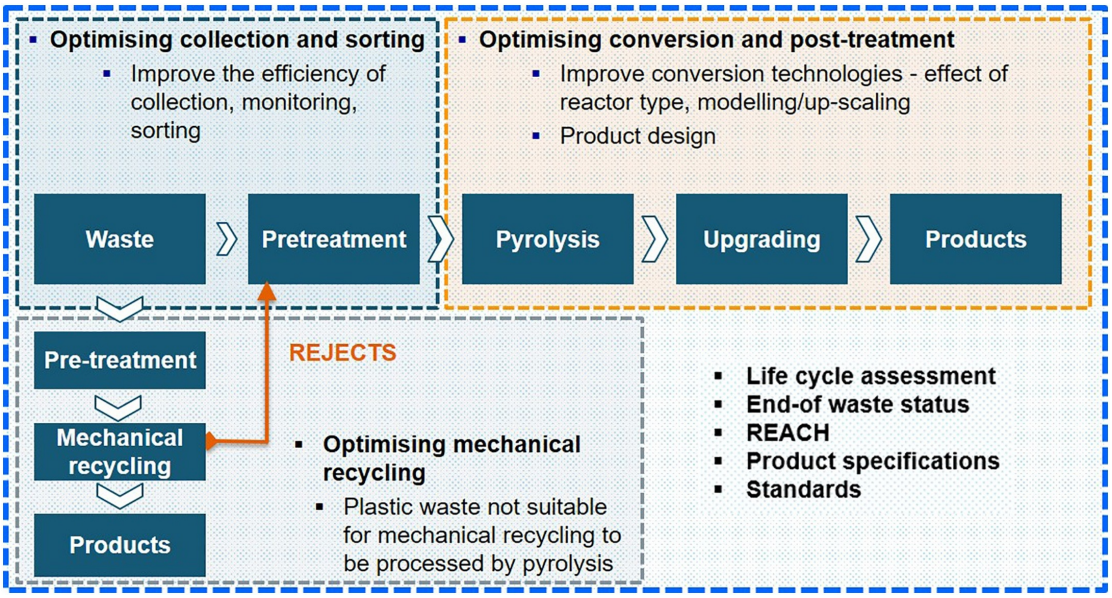

Figure 1.0.8: A combination with mechanical recycling and pyrolsis[23]

Lase et al [20] developed six potential scenarios for plastic waste treatment which include mechanical recycling, chemical recycling and solvent-based recycling (SBR). They have measured a set of circularity indicators to evaluate the effectiveness of each scenario. The best scenario based on these indicators, was a combination of mechanical recycling and chemical recycling, in addition to accounting for the "missing plastic". With this scenario, the end-of-life recycling can be improved from 18% to 80% and the plastic-to-plastic rate will be improved to 61%.

1.1 Pyrolysis

Pyrolysis is a type of thermolysis that has recently gained a lot of attention for its ability to recycle plastic. The pyrolysis process involves heating organic materials without oxygen, causing them to decompose [23]. As a result, the long-chain polymers break down into monomers, hence the plastic is converted to its original feedstock oil. Pyrolysis can be carried out with or without a catalyst, resulting in either thermal pyrolysis or catalytic pyrolysis. There are three different types of pyrolysis such as conventional/slow pyrolysis, fast pyrolysis, and ultra-fast/flash pyrolysis. Conventional/slow pyrolysis involves heating the material to a temperature of 400-500°C. The primary product in pyrolysis is the same as the distillation fractions in figure 1.0.4. when plastic is subjected to pyrolysis, it produces different fractions such as liquid oil, gases and char. The liquid oil fraction typically ranges from 31-39 %, while gases and char make up 2-47% and 0-16% respectively. The distillation fractions from pyrolysis vary from light oil (C_1-C_4) to heavy oil (C_{20}-C_{70}). The yield of liquid oil from plastic pyrolysis is influenced by factors such as volatile matter and ash content. The high volatile matter content in plastic makes it ideal for pyrolysis, as it favors the production of liquid oil. Conversely, the high ash content in plastic decreases the liquid oil yield. The main gas compo-

nents during pyrolysis are hydrogen, methane, ethane, ethene, propane, propene, butane and butene [19].

Since pyrolysis decomposes the plastic waste into feedstock oil, it is possible to produce plastic with the same value as virgin plastic. This also entails a higher tolerance for contaminations and the labor-intense sorting step is not necessary. Pyrolysis is a very flexible process that can be manipulated to obtain desired product distribution and yield adjusting temperature, residence time, pressure, different catalyst usage, and type of fluidizing gas. It is desirable to maximize the liquid fraction during the pyrolysis of plastic waste, in order to obtain a naphtha fraction for plastic production. The chemical properties of the plastic compounds, such as moisture content, fixed carbon, volatile matter, and ash content, are measured to ensure quality [19].

It is important to note that the various types of plastic produce varying mass balances, which can affect their suitability for pyrolysis. Figure 1.1.1 illustrates the mass balance that results from the pyrolysis of pure virgin plastic in a fixed-bed batch reactor at 700°C.

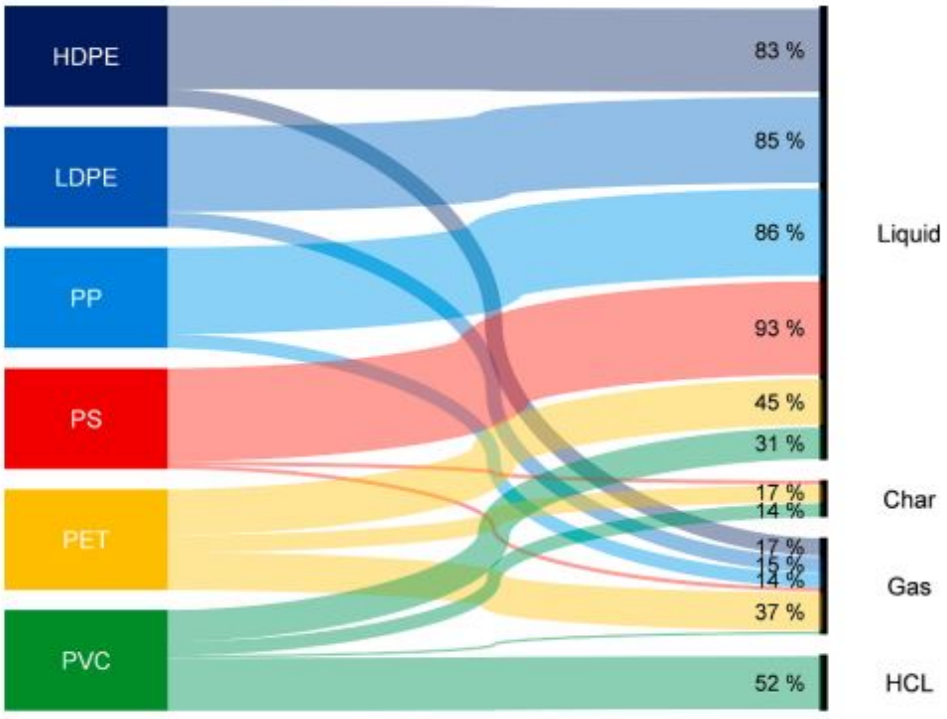

Figure 1.1.1: Mass balances from pyrolysis of pure virgin plastic in a fixed-bed batch reactor at 700°C [24].

As seen in figure 1.1.1, it can be observed that PET and PVC yield far less liquid through pyrolysis as compared to other plastics. While PVC results in around 50% HCl, PS yields a high amount of char and PET yields 37% gas. Therefore, the composition of the liquid depends on the amount of PVC, PET and PS present in the feedstock. As the aim is to maximize the liquid fraction, PVC, PET and

PS are less suitable for pyrolysis without any upgrading technologies.

The hydrocarbon composition is also dependent on the types of plastic in the feedstock, as illustrated in figure 1.1.2. The composition in figure 1.1.2 is an average of plastic waste pyrolysis conducted under various conditions.

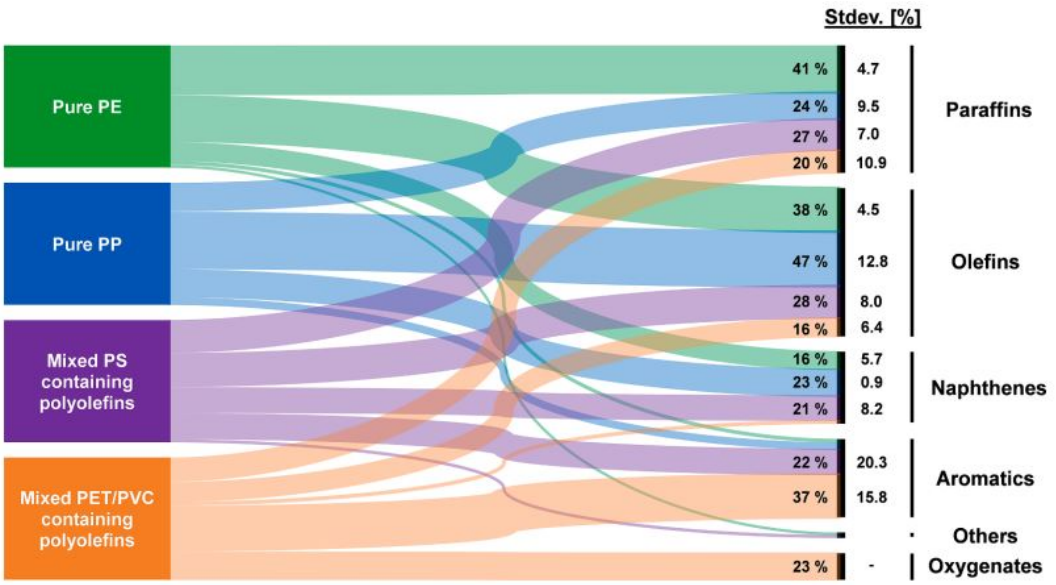

Figure 1.1.2: Hydrocarbon composition of different types of plastic [24].

As observed in figure 1.1.2, PS, PET and PVC produce high quantites of aromatics, while PP and PE produce more olefins. Additionally, PE, PP and PS are the top performers in terms of naphthenes production.

1.1.1 Factors affecting pyrolysis product distribution and yield

1.1.1.1 Catalysts

Catalysts speed up the chemical reaction and remain unchanged throughout the process. The operating temperatures can be lowered with the use of a catalyst, thus saving energy. Additionally, catalysts can improve the quality and selectivity of the reaction and remove contaminations [18]. There are two types of catalysts, homogeneous which is only one phase, and heterogenous which is more than one phase. A heterogeneous catalyst is preferred due to cost. Transition metals (Fe, Co, Ni and Cu) are generally good catalysts as they consist of two or more ion compounds. Typical heterogeneous catalysts used for plastic pyrolysis is acid based catalysts such as amorphous and mesoporous SiO_2 and SiO_2/Al_2O_3 catalyst, zeolites and FCC [19].

The amorphous and Mesoporous SiO_2 and SiO_2/Al_2O_3 is an acid catalyst with Bronsted acid sites and Lewis acid sites. A high ratio of SiO_2/Al_2O_3 of the catalyst, indicates a high strength of acidity. The advantage with SiO_2 and SiO_2/Al_2O_3

is that they tend to increase the liquid and gas yield. In addition, it favors a low degradation temperature and is coke-resistant. Zeolites are crystalline and microporous and the different ratios of SiO_2/Al_2O_3 indicate the acidity. In the opposite of SiO_2 and SiO_2/Al_2O_3, a low ratio indicates high acidity. The advantages of zeolites are that they are highly active due to their high specific surface area, the acidic sites improve the cracking reactions and they are stabilized in the catalytic cracking of crude oil. The disadvantages of zeolites are high cost and deactivation. FCC catalysts are zeolite crystals and a non-zeolite acid matrix known as silica-alumina with a binder. The main component is zeolite-Y. The advantages of FCC catalyst is that they are active, selective and accessible, attrition resistant, hydrothermally stable, high tolerance to metals, coke selectivity and fluid stability [19].

1.1.1.2 Temperature

The temperature is one important operating parameter and plays a crucial role in the polymer chain cracking reaction. It impacts the quantity and quality of the pyrolysis products, with higher temperatures resulting in shorter carbon cains and lower temperatures resulting in longer ones [25]. Moreover, increased temperature leads to higher char formation, while slow heating at lower temperatures leads to longer residence time and maximizes the char formation. The yield of gas is maximized at high temperatures and long residence times. Temperature also drives secondary reactions that can cause the formation of aromatic compounds. Different types of plastic exhibit different thermal behavior due to their varying structures, resulting in different decomposition temperatures during pyrolysis [19].The decomposition temperature range for the different types of plastic is summarized in table 1.1.1.

Table 1.1.1: Decomposition temperature range for different types of plastics. Summarized by Sharuddin et al [19].

Plastic types	Decomposition temperature range [°C]
PVC	220-520
PS	350-500
PET	350-520
PP	400-500
PE	400-500

A pyrolysis temperature at 300-500 °C is recommended in order to achieve the highest liquid yield with a feedstock of mixed plastic. With the usage of a catalyst, the temperature can be lowered. Temperatures above 500 °C was recommended if gaseous and char was to be preferred [19].

1.1.1.3 Pressure and residence time

The temperature has an impact on both pressure and residence time. Residence time is the average amount of time that the particle spends in the reactor, and a longer residence time results in a more stable product. When the temperature is high, a greater pressure leads to higher yield of gaseous products. At low pressure, the residence time is shorter which leads to less cracking of the polymer chain [19]. Residence time is also an important driver for secondary reactions, which causes aromatics [24].

1.1.1.4 Reactor

In plastic pyrolysis, batch, semi-batch, and continuous-flow reactors are commonly used, including fluidized bed, fixed-bed, and conical spouted bed reactors [19].

1.2 Contaminations

Although pyrolysis has the ability to handle more contamination than mechanical recycling, it still poses a challenge. To produce suitable pyrolysis oil from plastic waste, the oil must be compatible with industrial steam cracking units. This requires measuring physical properties such as molecular composition and potential contamination limits. Post-consumer waste consists of unknown compositions and various contaminants. These contaminants can come from additives, organic materials (such as food remains), and inorganic materials (like inks) [24].

The most common heteroatom contaminants in plastic waste are nitrogen, oxygen, chlorine, iron, sodium and calcium. Figure 1.2.1 displays the concentration level of some of these contaminants in the light, medium and heavy distillation fractions resulting from the pyrolysis. The red values in figure 1.2.1 indicate the contamination limit threshold for industrial steam crackers, as established by Kusenberg et al[24].

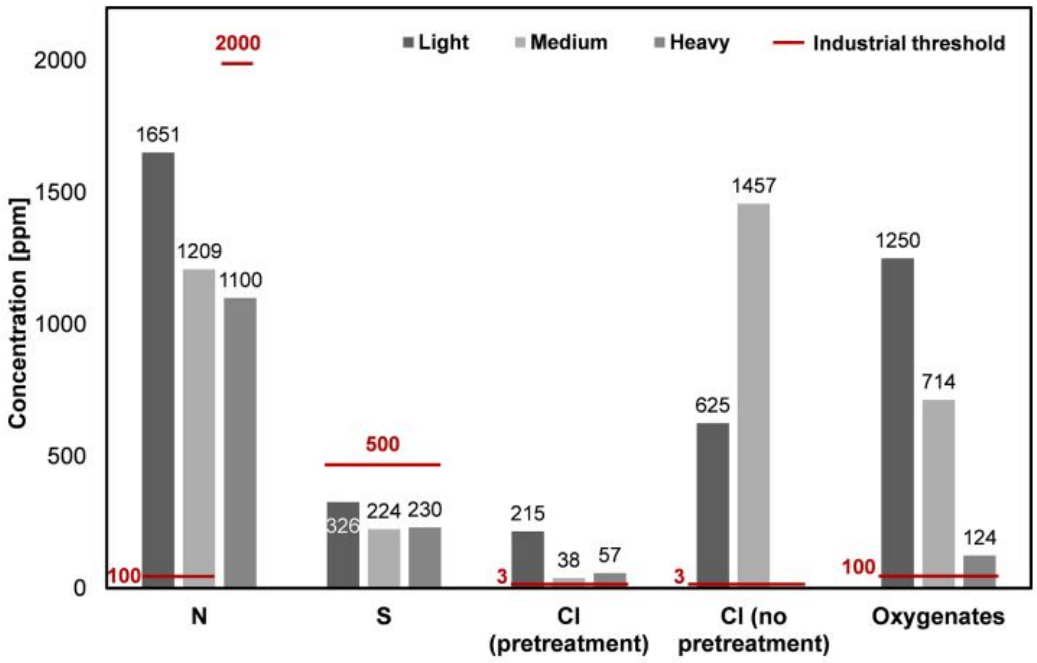

Figure 1.2.1: Overview of the heteroatom content in the light, medium and heavy fractions compared with tha reshold value for the industrial steam crackers. The values are taken from Kusenberg et al [24].

As seen in figure 1.2.1, the contaminations are exceeding these limits in the industrial steam cracker units. To ensure compatibility with physical properties such as viscosity, boiling point, molecule composition, and potential contaminant limits, it is necessary to upgrade and/or pretreat the fractions from pyrolysis in the liquid feedstock. Kusenberg et al [24] have identified the most problematic contaminants and their limits, which are summarized in table 1.2.1.

Table 1.2.1: Specific contaminant limits for steam cracking. Values taken from Kusenberg et al [24]

Compound	**Limit [ppm]**
N	100
O	100
Cl	3
Fe	0.001
Ca	0.5
Na	0.125

Excessive levels of various contaminants can lead to multiple issues. Nitrogen content, in particular, can render the catalyst ineffective. Additionally, thermal decomposition may result in the production of NO_x, leading to air pollution and acid rain. The decomposition of nitrogen-based compounds creates ammonia and nitriles, which can be detrimental to downstream catalysts. A viable solution to eliminate nitrogen content is hydrodenitrogenation. When oxygen reacts with

certain compounds, such as butadiene, it can lead to the formation of unwanted byproducts like methanol, formaldehyde, CO, and corrosive acids. This can decrease the value of steam cracking feedstock and cause problems with process fouling and corrosion. Additionally, the decomposition products of oxygen can be harmful to catalysts downstream of steam crackers. To prevent these issues, it is recommended to remove oxygen through hydrooxygenation. A commonly used additive for improving performance is $CaCO_3$, which contributes to the calcium content in the feedstock. However, calcium can lead to issues such as fouling and corrosion. To address this, a calcium removal agent can be used in an aqueous solution to eliminate the calcium content. Iron contamination can have negative effects on furnace performance, including the formation of coke and reduced run length, as well as corrosion and catalyst poisoning. Additionally, the formation of iron oxide can lead to plugging issues. To mitigate these problems, hydrometallization, solvent extraction, or membrane filtration techniques can be employed to remove iron. Excessive presence of sodium can lead to corrosion and also act as a potent catalyst poison and coke promoter. One possible solution to meet the prescribed sodium limits in the feedstock oil is to blend it with 15 wt% naphthas. Chlorine content can result in the creation of both organic and inorganic chlorides. Among these, HCl is the main organic chloride and can bring about severe corrosion in downstream facilities, as well as the formation of ammonium chloride with nitrogen, causing blockages. When in contact with a catalyst, HCl can also deactivate it. Furthermore, chlorine contamination can lead to environmental concerns. As seen in figure 1.1.1, PVC plastic yields about 50% of HCl. Due to the low limit of chlorine contamination, as indicated in Table 1.2.1, hardly any PVC is allowed in plastic waste fractions. Removing the chlorine from the feedstock with a good dechlorination method is therefore important in order to make PVC plastic more suitable for pyrolysis. It is more difficult to detect and separate the organic chlorides [24].

Besides heteroatom pollutants, the liquid feedstock can also be tainted with aromatics and olefins. When their concentration is too high, they can trigger coke buildup and fouling. Olefins can even lead to blockages in the reactor tubes by starting polymerization reactions. To avoid these issues, it is recommended to eliminate plastics with high levels of aromatics before steam cracking [24]. Figure 1.1.2 displays the hydrocarbon composition of various plastic types.

In order to eliminate heteroatom contaminations, aromatics, and olefins, it is crucial to upgrade technology and pre-treatment methods. Pyrolysis is more influenced by PS, PET and PVC due to the formation of HCl, aromatics and olefins. Different methods and technologies are suitable for different types of plastics. To find the method which optimizes the desired product such as naphtha in terms of cost is necessary. For many of the heteroatom contaminants, hydrotreatment is a popular technology [24].

1.2.1 Dechlorination

One method of removing chlorine is through dechlorination. The use of PVC plastic material is increasing due to its low cost and high performance, making it one of the most commonly used plastics [26]. As a thermoplastic, it can be melted using heat, making it a potential candidate for chemical recycling via pyrolysis. However, due to its high chlorine content, an efficient dechlorination step is required for it to be suitable. PVC plastic contains over 50% of chlorine, which results in the formation of HCl and chloroorganic compounds during pyrolysis [19]. These compounds are formed in two steps, with most of the chlorine being eliminated during the first step. However, even a small amount of 1% can create chloroorganic compounds. Given the high usage of PVC plastic and the fact that even 1% of chlorine can lead to the formation of these compounds, overcoming the limitation of chlorine content in the oil is crucial [27].

The first step of thermal decomposition of PVC takes place at temperatures below 360°C, resulting in the realase of HCl gas. The second step occurs above 360°C [28] and leads to the fromation of chloroorganic compounds [24]. The thermal decomposition of PVC are shown in figure 1.2.2.

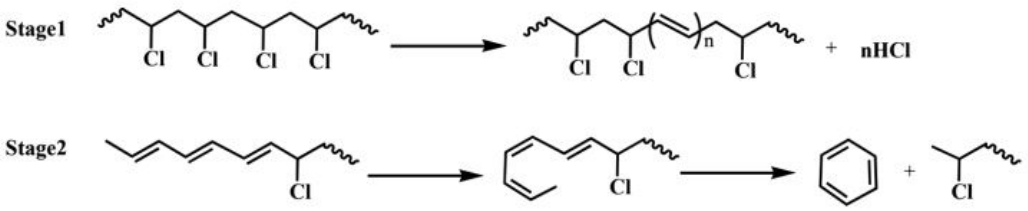

Figure 1.2.2: Thermal decomposition mechanism of PVC [24]

Difference from dehydrochlorination, dechlorination is the process of eliminating chlorine without the presence of hydrogen [27]. There are three methods for dechlorination, which include stepwise dechlorination, sorbent in-situ, and the use of sorbent, catalyst, and/or H_2 in ex-situ. In-situ dechlorination occurs within the reactor, whereas ex-situ dechlorination takes place outside the reactor. Stepwise pyrolysis involves a pre-dechlorination step before the pyrolysis step, which removes HCl from the oil at a lower temperature. This minimizes the HCl in the second step, where the temperature is increased, and reduces the formation of chloroorganic compounds. Using sorbents in-situ or ex-situ can capture chloroorganic compounds and/or HCl. Different combinations of these possibilities could be a solution. Combining stepwise pyrolysis with a sorbent can separate the HCl gas from the sorbent, and decrease the formation of chloroorganic compounds. Various combinations of these methods can be used as a solution to the problem. [29].

1.2.2 Sorbents for dechlorination

Sorbents is a material which is used for absorbtion or adsorption. Typical sorbents for dechlorination is Fe-based, Na-based and Ca-based sorbents. Iron is a well known catalyst/sorbent and has various valences such as 0, +2 and +3. Iron can exist as Fe^0, FeO, Fe_2O_3 and Fe_3O_4 [30].

1.2.2.1 Red mud

Among iron-based materials, red mud can be a good candidate in the dechlorination process. Red mud has a high content of Fe_2O_3, specifically 30-60%. Red mud is a bauxite residue from aluminum production and is a very fine-grained material. As red mud is a residue of alumina production, it is also very cheap. In addition to Fe_2O_3, red mud contains multiple other components. The composition of red mud can vary depending on the source of bauxite, the processing method and the processing conditions. However, there are certain common components present in all types of red mud. The major elements and minerals in red mud are shown in table 1.2.2.

Table 1.2.2: The major elements and minerals in red mud [31]

Major elements		**Major minerals**		
Composition	**composition [%]**	**Minerals**	**Chemical formula**	**Composition [%]**
Fe_2O_3	30-60	Sodalite	$3Na_2O3Al_2O_36$-$SiO_2Na_2SO_4$	4-40
Al_2O_3	10-20	Cancrinite	$Na_3CaAl_3Si_3O_{12}$-$2CO_3$	0-20
SiO_2	3-50	Aluminous-goethite	α- (FeAl)OOH	10-30
Na_2O	2-10	Hermatite	Fe_2O_3	10-30
CaO	2-8	Silica	SiO_2	5-20
TiO_2	-	Tatium dioxide	TiO_2	0-10
		Perovskite	$CaTiO_3$	0-15

Iron oxides present in red mud give it a red color. Every year, about 150 million tonnes of red mud are produced globally. However, disposing of this waste is a major challenge due to its high pH value, which ranges between 10 and 13, primarily due to high concentrations of NaOH. Currently, the most common method of dumping red mud is dry stacking, which results in environmental pollution due to the dry and dusty nature of the mud. Moreover, red mud contains soluble compounds like sodium carbonate, sodium hydroxide, and sodium bicarbonate that dissolve with rainwater and pollute land and rivers. Therefore, it is vital to explore more suitable applications for red mud [31].

Each year, it is estimated that around 20 million tons of iron from red mud go to

waste. The fact that red mud is a waste, makes it an attractive option due to low cost. However, the surface area of red mud is relatively low, ranging from 10-30 m^2/g. To enhance the catalytic efficiency of red mud, it may require activation or pre-treatment depending on its application. This could involve heat treatments to remove impurities such as FeOOH and $Al(OH)_3$ and reduce the iron phases to increase activity. It may also be necessary to remove Na and Ca, as sodium promotes sintering, which reduces the specific surface area at high temperatures[31].

Figure 1.2.3: Red mud in Greece. Taken by Casper Van der Ejik [32]

1.3 Objectives

The objective of this thesis has been to achieve a reduction of the chlorine content of the real light oil fraction obtained from Quantafuel, from 55 ppm to 10 ppm, with gas dechlorination. Specifically, the thesis has focused on investigating the Fe-based residue, red mud, in the dechlorination of a model compound, chlorobenzene. Chlorobenzene was selected as the model compound due to its well-known complexity of dechlorination, particularly when compared to linear aromatics. The effect of washing red mud with HCl has been investigated in order to determine the influence of other components in red mud, such as na-based and ca-based, on the dechlorination reaction. Further, the investigation has been carried out with different experimental conditions. The effect of regeneration on the different experiments has also been investigated.

1.4 Litterature review

1.4.1 Pyrolysis

As previously discussed, the real world plastic waste contains of a variety of plastic types, resulting in a complex composition that is further complicated by contaminants. Pyrolysis is a viable solution as it has the ability to effectively manage contaminants. However, due to the low liquid yield for PVC and PET plastic, in addition to the high yield of HCl from PVC, seen in figure 1.1.1, PVC and PET plastic is less suitable for pyrolysis without any upgrading technologies or pre-treatments.

From numerous authors, it is seen that the dechlorination step occurs at low temperatures, such as 250-320°C [33][34][19][29]. At this temperature, HCl is formed and leads to complications in the steam crackers due to the subsequent formation of chloroorganic compounds. Thermal degradation for some plastics requires a higher temperature, as seen in table 1.1.1 than the dechlorination temperature, making lower temperature ineffective in these circumstances. Miranda et al [33] investigated the thermal decomposition of PVC in vacuum pyrolysis with a temperature range from 225-520°C. The investigation illustrates that the liquid yield is relatively low across the temperature range. At 360°C, the liquid yield was 3.9%, and at 520°C, the liquid yield was increased to 12.79%. The main yield from pyrolysis of PVC plastic is HCl, which ranges from 44.35% to 58.20% across the temperature range. At 520°C, the tar formation is relatively high with 19.60%.

The purpose of conducting investigations utilizing catalytic pyrolysis is to optimize liquid oil production and its properties, as well as reduce operating temperatures. A range of catalysts has been utilized in plastic waste pyrolysis, including red mud, fluid catalytic cracking (FCC), ZSM-5, HZSM-5, Y-zeolite, Fe_2O_3, Al_2O_3, $Ca(OH)_2$ and natural zeolite. However, Lopez et al [35] and Lopez et al [29] show that the thermal decomposition of plastic yields a higher liquid yield, compared to thermal decomposition with a catalyst.

Lopez et al [29] investigated a combination of catalytic and stepwise pyrolysis with PE, PP, PS, PET and PVC as feedstock and ZSM-5 as catalyst. A conventional catalytic process was also performed at 440°C for comparism. Two different combinations of catalytic and stepwise pyrolysis were carried out. In one of the combinations, the catalyst was mixed with the plastic in both steps, whereas in the other combination, the catalyst was only added in the second step. The first step in the stepwise pyrolysis was carried out under 300°C and the second step was carried out under 440°C. It was observed that the addition of catalyst in both steps resulted in comparatively lower reduction in the liquid yield, when compared to the addition of the catalyst in both steps. A suggested conclusion from Lopez et al [29] was that the hazardous HCl gas causes a decrease in liquid yield due to deactivation. This suggests that the addition of a catalyst in the second step alone can be more efficient. However, for the light fraction (C_5-C_9), the yield was slightly increased (from 81.5% to 82%) for the addition of catalyst in the second step. This implies that the catalyst actually works. Lopez et al [35] investigated

pyrolysis of a mixture of plastic containing PE, PP, PS, PET and PVC with ZSM-5 and red mud as a catalyst. The investigation shows that the highest liquid yield was achieved with thermal pyrolysis. The addition of catalysts increases the gas fraction and lowers the liquid fraction. Red mud yields a higher liquid fraction, compared to ZSM-5. However, the Red mud needs a higher temperature, due to negotiable activity under 500°C.

In addition to the lower liquid yield, it is seen that aromatic substances are increased with the usage of ZSM-5 as catalyst[29][35]. Lopez et al [35] concluded that the strong aromatization is due to the strong acidity of the HZSM-5. Strong acid sites contribute to coke-formation reactions and further to fast deactivation. However, Lopez et al [29] concluded that the ZSM-5 catalyst is a good option for plastic pyrolysis because it is shown that it is a catalytic effect as long as deactivation from HCl can be avoided. In addition, an argument was that a pure aromatic liquid fraction is more valuable than a mixture of aromatics and olefins. Compared to ZSM-5, red mud contain both weak and strong acid sites due to Al_2O_3 and SiO_2 which should be taken into account due to need for higher temperature for red mud. In addition, it is seen by Ermakova et al [36], that some Na_2O components can act as poison and diminish the catalytic activity. This effect can influence the activity of red mud, due to the na-content in red mud.

Despite the decrease in liquid yield observed in the investications from Lopez et al[29] and Lopez et al[35], it has been determined that the catalyst employed in pyrolysis is working. However, a noticeable problem that may be contributing to this decrease is the deactivation of the catalyst by HCl. Furthermore, it has been seen by Miranda et al [33] that the effect of catalysts in stepwise pyrolysis lower the required operating temperature, hence lower consumption of energy is required.

1.4.2 Dechlorination

It is crucial to discover an economical and highly effective dechlorination technique to remove chlorine contamination and improve the liquid yield from PVC plastic. Numerous dechlorination techniques have been studied to remove chlorine from plastic waste and increase the liquid yield in pyrolysis oil.

To comprehend the dechlorination mechanism, the utilization of a model mixture can prove to be beneficial. Jiang et al [37] investigated the thermal effect on dechlorination of chlorinated hydrocarbons with a model mixture consisting of iso-octane doped with aliphatic substances, specifically 2-chlorobutane, 2-chloroethylbenzene, as well as the aromatic substance, chlorobenzene. This study aimed to examine the influence of thermal treatment in the presence and absence of a sorbent. The sorbent employed in the investigation were Na_2CO_3 and $CaCO_3$/Al. The proposed mechanism by Jiang et al is presented in equation 1.1 - 1.3.

$$C_4H_9Cl \rightarrow C_4H_8 + HCl \tag{1.1}$$

$$C_8H_9Cl \rightarrow C_8H_8 + HCl \tag{1.2}$$

$$C_6H_5Cl \rightarrow C_6H_6 + HCl \quad (1.3)$$

From the study on the thermal effect with the absence of a sorbent, the results show that 2-chlorobutane has a maximum conversion to 2-butene at 350°C. For 2-chloroethylbenzene, the conversion is 30% of the inlet concentration at 400°C. Chlorobenzene is not decomposed until the temperature reaches 500°C. Clearly, a thermal decomposition of chlorobenzene is more difficult. The higher temperature for decomposition of chlorobenzene is supported by other authors as well[38][39].

As earlier mentioned, the removal of chlorine through thermal treatment is primarily in the form of HCl, as represented by equation 1.1 to 1.3. Jiang et al[37] observed that the dechlorination temperature is significantly reduced with the presence of sorbents. The dechlorination temperature for 2-chlorobutane and 2-chloroethylbenzene was decreased to 180°C. For chlorobenzene, it was observed that the dechlorination temperature was decreased to 450°C. It was also seen that the breaktrough time for chlorobenzene is shorter, compared to 2-chlorobutane and 2-chloroethylbenzene. A suggested conclusion was that the adsoprtion of chlororbenzene proceeds mainly on the surface of Na_2Co_3 and the dechlorination chlororbenzene takes place with direct interaction with Na_2CO_3 because of the larger molecular size, compared to HCl.

From the investigation done by Jiang et al‘[37] it is seen that the dechlorination is improved with the absence of a sorbent/catalyst. Several investigations have also mentioned that various sorbents, including $CaCO_2$, $Ca(OH)_2$, CaO, Na_2CO_3, Fe_3O_4 and Fe have been efficient during dechlorination. Investigations have been done with different combinations of the three possibilities for dechlorination. Investigations done by Jan Hubáček et al [28] and A. López et al [40] with sorbents in-situ were seen to increase the chlorine content in the liquid yield. The explanation for the increase of the chlorine content in the liquid yield was that Cl probably was adsorbed by the sorbent initially, but as the pyrolysis temperature exceeded 400°C, part of Cl was desorbed and reacted with hydrocarbons to form chloroorganic compounds. Keeping the pyrolysis temperature below 400°C could be insufficient for some plastics. In addition to the investigation carried out with in-situ sorbent, Jan Hubáček et al carried out investigations done with stepwise pyrolysis and sorbents in ex-situ, such as $Ca(OH)_2$-extrudate, Fe_3O_4 in silica and Fe_3O_4 in silica reduced at 600°C. The feedstock was a model mixture of 5 types of plastics (5P), which included 10% PVC. The main components after the reduction were seen to be Fe^0 and Fe_2SiO_4. For the stepwise pyrolysis, the first step was carried out under 350°C and the second step was carried out under 500°C. In conclusion, it was predicted that Fe^0, Fe_3O_4 and $Ca(OH)_2$ were efficient for dehalogenation at 300°C. However, the best result was obtained with Fe_3O_4−Si, which decreased the Cl content in the liquid yield to 3-23 ppm, which corresponds to 98.9% efficiency. The limit for the steam cracker for the research was 10 ppm. The reduced Fe_3O_4 sorbent in silica did not improve the dechlorination efficiency further. Jan Hubáček et al explained this by the sintering effect and significant decrease in sorbent surface area after reduction.

However, the real plastic waste is more complex than the model mixture. Jan Snow et al [41], investigated catalytic dechlorination with MPW (municipal plas-

tic waset) and detected that the dechlorination efficiency with sorbents decreased, compared to pyrolysis of a model plastic mixture. It was seen that the chlorine content was relatively low in the MPW. After pyrolysis with MPW, the liquid averaged 294 ppm chlorine. In addition to the complex mixture, these findings could not be definitively determined. Jan Snow et al investigated the stepwise pyrolysis in combination with ex-situ sorbents such as $Ca(OH)_2$-extrudate, Fe_3O_4 in silica, Fe-Si, hydrotalcite (MgO) and β-zeolite. The first step was carried out under 350°C and the second step was carried under 500°C. The best yield was achieved with hydrotalcite and β-zeolite, which was 95% efficient. The efficiency of $Ca(OH)_2$-extrusion was the lowest, followed by Fe_3O_4 in silica and Fe-Si. Compared to dechlorination with the model mixture as feedstock, the efficiency decreased respectively 48%, 31% and 14% for the sorbents. It was also seen that the duration time for the step had an impact on the chlorine content. The efficiency was increased from 38% to 68% with an increase from 1 to 2 hours in the first step with MPW as feedstock. However, with an 1 hour long step with the 5P mixture, the efficiency was 99%. Based on the results, it was also suggested that PET acts negatively as chlorine-binding agent during stepwise pyrolysis of PVC-containing feedstock.

As earlier mentioned, the HCl gas can deactivate the catalysts. Lingaiah et al [42] have investigated the effect of iron oxide-carbon composite catalyst on the dechlorination and found that by continuously flowing He, the adsorbed HCl would be removed and the deactivation of the catalyst was overcome. It has been suggested that the process begins with iron oxide acting as a catalyst to generate HCl. The HCl is then absorbed by the iron oxide, which deactivates the catalyst. This absorption process results in the formation of iron chloride, which once again serves as a catalyst for the dechlorination of chloroorganic compounds. The different catalysts for the investigation were γ-Fe_2O_3, α-Fe_2O_3, TR97305 and TR99300. TR97305 and TR99300 are Fe_3O_4 catalysts, but prepared by different methods. The feedstock was a model mixture of plastic, containing 1%PVC. The dechlorination was carried out under 350°C. The TR97305 catalyst shows an initial conversion of 100%, followed by a gradual decrease to 60%. Following regeneration, the conversion for the catalyst is initially 80% for the two subsequent cycles. This rate drops to approximately 40%. Lingaiah et al found that the removal of chlorine compounds is very high with lower space velocities. From XRD analysis after the investigations, it was observed that the XRD patterns were not changed.

1.4.2.1 Red mud as sorbent

Red mud has been studied as a potential sorbent for dechlorination, due to the high content of Fe_2O_3 and low cost. However, there are some problems associated with its use. One issue is that the effectiveness of red mud as a sorbent can be limited by its low surface area and poor porosity. Another problem is that red mud may contain impurities that can interfere with the dechlorination process or even cause further contamination. Additionally, red mud may require pretreatment or modification to optimize its performance as a sorbent. Despite these challenges, research is ongoing to explore the potential of red mud as a sorbent.

Wang et al [43] investigated the calcination temperature from 400-900°C and the XRD profile for the different calcination temperatures are seen in figure 1.4.1
.

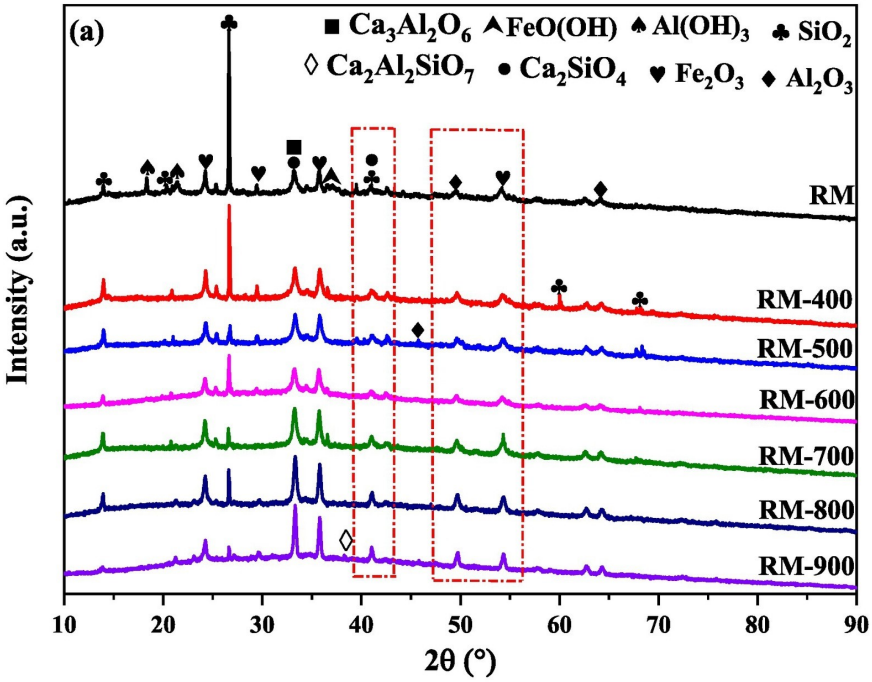

Figure 1.4.1: XRD profiles for red mud at different calcination temperatures. Taken from Wang et al [43]

Based on the XRD profile in figure 1.4.1, it can be seen that a calcination temperature above 500°C removes components such as FeO(OH), $Al(OH)_3$ and $Ca_3Al_2O_6$. These components were decomposed to Fe_2O_3 and Al_2O_3 due to oxidation. They suggest that an optimal calcination temperature is 400-600°C. At the specified temperature range, the specific surface area increased. From N_2 adsorption-desorption isotherms, it was determined that the pore size of red mud fell within the mesoporous range. In the same study, Wang et al [43] investigated the calcination temperature for Ni-supported red mud. They observed that temperatures above 700°C could trigger the sintering of metal oxides and cause a collapse of pore structure, which further leads to a decrease in the surface area.

As seen in table 1.2.2, iron in raw red mud do mainly exist as Fe_2O_3. By reducing Fe_2O_3, a higher yield of electrons can be attained, resulting in greater efficiency in promoting chemical reactions. The various oxidation states have been investigated, with the aim of increasing the activity. Ordóñez et al [44] have investigated the reduction of red mud with TPR studies. Figure 1.4.2 displays the TPR profile.

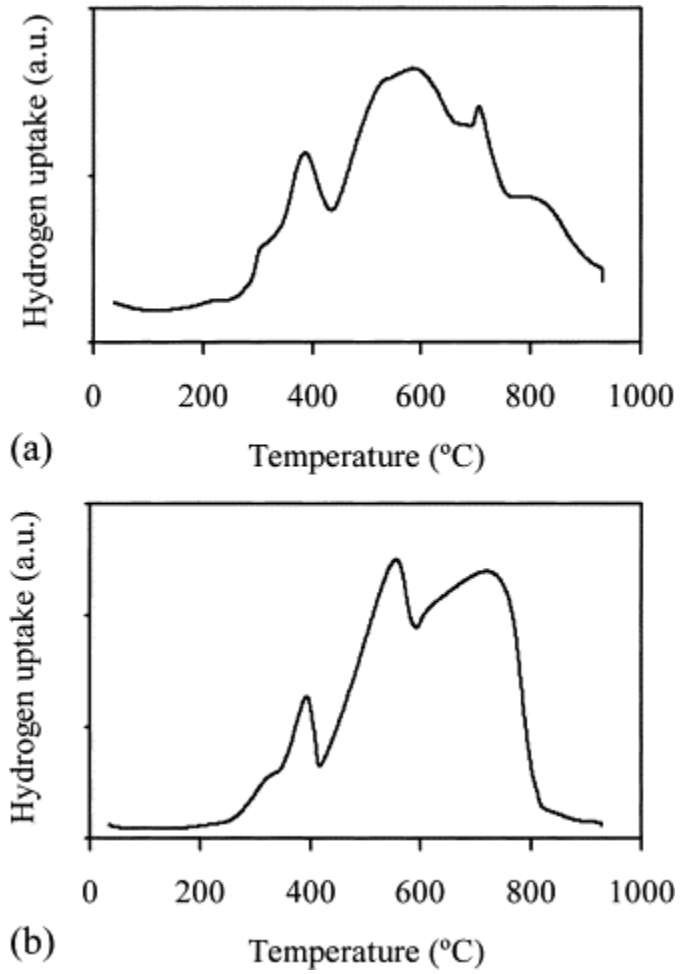

Figure 1.4.2: TPR profiles for: (a) red mud and (b) $\alpha - Fe_2O_3$ [44]

The reduction of Fe_2O_3 to Fe takes place via $Fe_2O_3 \rightarrow Fe_3O_4 \rightarrow FeO \rightarrow Fe^0$. The TPR profile of Fe_2O_3 in figure 1.4.2 (b) shows three distinctive peaks. Similar peaks have been observed in the TPR profile of red mud in figure 1.4.2 (a). These observations have led to the conclusion by Ordóñez et al [44] that these peaks correspond to the three steps involved in the reduction of Fe_2O_3 and that it is unlikely that other elements in red mud are reduced. The first peak is around 400°C and corresponds to the reduction from Fe_2O_3. The second and the third peak is around 450°C to 850°C and correspond to the reduction to FeO and Fe.

Multiple authors claim that acid treatment could also contribute to an increase in activity. Investigations state that treatment of acid increases the surface area. The treatment of acid decreases the content of sodium and calcium. A dissolution/precipitation process with HCl and ammonia carried out by Kerry et al [45] show that the specific surface area was increased from 64 m^2/g to 155 m^2/g. Parades et al [46] dissolved red mud in a mixture of HCl and H_3PO_4, which lead to an increase from 28.3 m^2 to 111.7 m^2/g in the specific surface area. Altundoğan et al [47] increased the adsorption capacity of red mud by treating it with HCl. The treatment lead to the removal of sodalites. Altundoğan et al suggested that the increased adsorption capacity is likely due to the removal of these sodalite compounds, which may have previously blocked active sites on the sorbent. In

addition, Sushil et al [48] does also suggest that sodium and calcium contribute to poor activity, because they promote sintering and hence decrease the surface area. They studied the catalytic combustion of methane with red mud and saw that red mud treated with HCl had an increase in activity. The best activity was obtained with Fe_2O_3 as a catalyst, which was calcined at 600°C. In addition, the surface area was increased from 28.3 m^2/g to 131.1 m^2/g.

Even though it is seen that treatment with acid increases the activity, deactivation in the catalysts has been observed. The investigation with red mud by combustion of methane by Parades et al [46] shows a deactivation in the catalyst even treated with HCl, although the activity is better than the untreated sample. The sample treated with HCl shows a similar result as the pure hematite on a Fe content basis. Parades et al suggest that the deactivation is mainly due to a decrease in the surface area due to sintering and transformation of hematite into less active phases. However, it has been observed that some sorbents, such as Fe_2O_3 adsorbs the HCl which causes deactivation for the catalyst.

CHAPTER

TWO

THEORY

This part explains the theoretical aspects of reaction chemistry, as well as the preparation steps and characterization of sorbents. This information is crucial for the upcoming experiments.

2.1 Reaction chemistry

2.1.1 Dechlorination reaction

Compared to linear aromatic, chlorobenzene is known for its complexity of dechlorination. The dechlorination reaction chemistry of chlorobenzene with a Fe-based material is shown in figure 2.1.1.

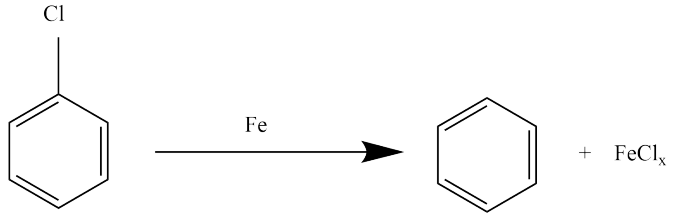

Figure 2.1.1: Dechlorination of chlorobenzene with iron.

Chlorine is adsorbed by iron and converted to chlorobenzene and iron chloride ($FeCl_x$). The state of iron chloride is dependent on the experimental conditions, as well as the Fe-based material provided in the reaction.

2.1.2 Reduction chemistry

Reduction is the loss of electrons and iron oxides can be reduced by flowing hydrogen. The reaction scheme of the reduction from Fe_2O_3 to Fe^0 is seen in equation 2.1 to equation 2.4.

$$3Fe_2O_3 + H_2 \rightarrow 2Fe_3O_4 + H_2O \tag{2.1}$$

$$Fe_3O_4 + H_2 \rightarrow 3FeO + H_2O \tag{2.2}$$

$$FeO + H_2 \rightarrow Fe + H_2O \tag{2.3}$$

$$Fe_2O_3 + 3H_2 \rightarrow 2Fe + 3H_2O \tag{2.4}$$

2.1.3 Regeneration reaction

Iron can be reused, by regenerating it back to its original form. This can occur by reacting $FeCl_x$ with air as described in equation 2.5.

$$FeCl_x + O_2 \rightarrow Fe_2O_3 + Cl_x \tag{2.5}$$

2.2 Preparation of sorbent

2.2.1 Incipient wetness method

Impregnation is one of the most commonly used techniques for the synthesis of heterogenous sorbents. The sorbent is dissolved in an aqueous or organic solution. When the sorbent is fully dissolved, it is added to the catalyst support drop by drop. Due to capillary forces, the solution is drawn into the pores. On the opposite of wet impregnation, the incipient wetness method limits the solution amount to just fill the pores to saturation. The wetness method leaves excess liquid and the solution needs to be filtrated. The solution is drawn into the pores due to capillary forces. Further, the sorbent is dried and calcined to produce impregnated pellets and remove volatile components [49].

2.2.2 Calcination

Calcination is heating of solid material with a controlled temperature. This process removes impurities and volatile substances and is essential to yield the desired qualities. Calcination can prevent the impurities to poison the catalyst, and helps controlling the surface area, locking the pore structure, securing the crystallization phase and activaties the wetting and spreding [50].

2.2.2.1 Passivation

Passivation is a chemical treatment which create a layer outisde of the material to make the surface less reactive. This layer is created when the sample is exposed to air and prevents further oxidation and corrosion in room-temperature [51].

2.3 Characterization techniques

2.3.1 Temperature programmed reduction (TPR)

TPR is a technique for the characterization of solid materials, particularly in the context of determining their reduction temperature. The process involves placing a solid material in a specialized reactor and heating it while flowing hydrogen gas over it. The hydrogen consumption is recorded and displayed as a function of the temperature [52]. The data can be used to determine the reduction temperature. A general reduction reaction between a metal and hydrogen is represented

in equation 2.6.

$$MO(s) + H_2(g) \rightarrow M(s) + H_2O(g) \tag{2.6}$$

2.3.2 X-ray powder diffraction

X-ray powder diffraction (XRD) is a structural analysis and a bulk measurement technique. This technique is used to identify phases in crystalline materials. A crystalline material contains of atoms with well-defined distances, d. By exposing the sample to X-ray energy, the electrons will adsorb the energy and release the energy in the form of a new X-ray called diffracted X-ray. The incident x-ray and the diffracted x-ray create a specific angle as seen in figure 2.3.1.

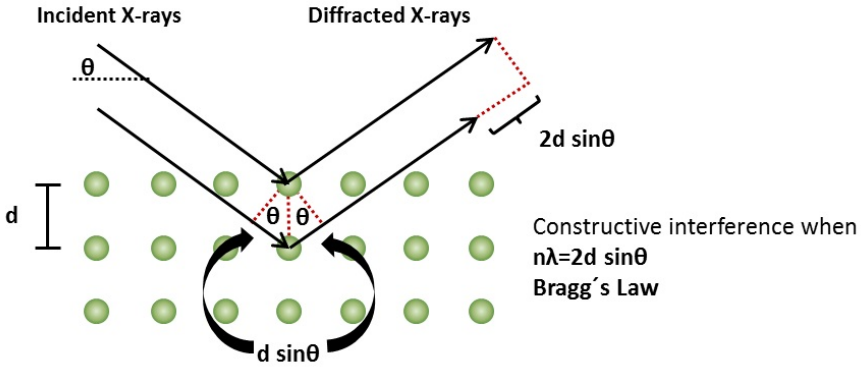

Figure 2.3.1: Schematic illustration of the Bragg equation [53]

X-ray is high energy light with a repeating period called wavelength, λ. This diffraction pattern is produced when the sample is exposed to X-ray as seen in figure 2.3.1, and can be used to determine the phases in the bulk.

The relationship between the angle and the wavelength is described in Bragg's law, which is shown in equation 2.7.

$$n\dot{l} = 2\dot{d}\sin\theta \tag{2.7}$$

The phases in the sample can be analyzed from a graphical presentation of the intensity versus $2{\cdot}\theta$. A detector in the XRD will record the number of x-rays observed at each angle 2θ, where the intensity is recorded as "counts" or "counts per second". In addition to determining the crystal phases in the bulk, the XRD peaks can provide detailed information about the crystal structure and properties of a material. The peak position corresponds to the spacing between atomic planes in the crystal lattice, while the peak intensity is proportional to the number of atoms in the crystal structure. The peak width provides information about the size and quality of the crystalline domains in the sample. Each peak in an XRD pattern corresponds to a particular crystal structure and orientation. A single crystal would produce one peak in the diffraction pattern. A polycrystalline would produce peak for every set of planes [53].

2.3.3 X-ray Fluorescence

X-ray Fluorescence (XRF) is used to determine the elemental composition of materials and the quantity of the element in the bulk. By striking the inner shell electron, such as the K shell, with a primary x-ray, the electron will be released as a photoelectron. X-ray is a form of high-energy electromagnetic radiation and needs to be higher than the binding energy in order to release the electron. The atom will be unstable when an electron from the inner shell is released. To stabilize the atom, an electron from an outer shell will be pulled to the vacant spot created when the electron irradiated with x-ray was released. When an electron is moving from an outer shell to the vacant spot, a new x-ray will be emitted as an x-ray fluorescence radiation. This x-ray is unique for each atom. The elemental composition and its quantity can be analyzed from a graphical presentation of x-ray intensity peaks versus wavelength. The peak height/intensity indicates its concentration [54]. Figure 2.3.2 show an illustration of the electron and the x-ray fluorescence radiation being released when striking the electron in the inner shell with x-ray.

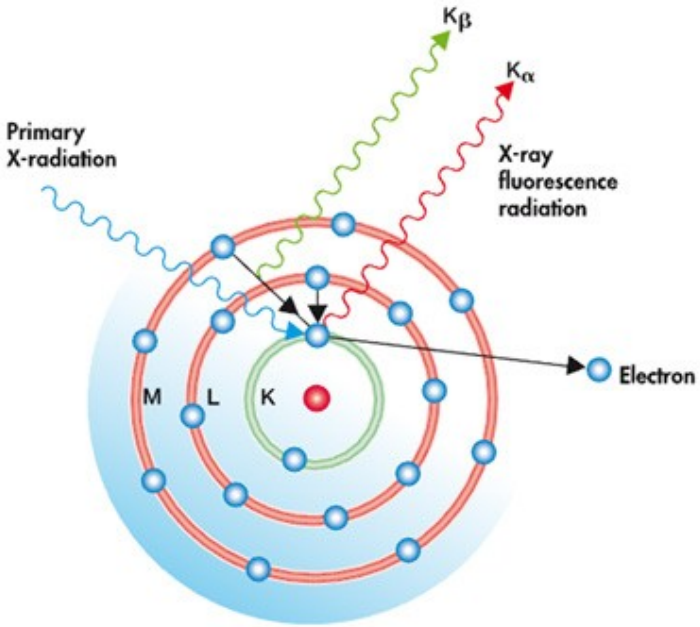

Figure 2.3.2: Atmoic model for the X-ray Fluorescence analysis method [55]

2.3.4 Thermogravimetric analysis

Thermogravimetric analysis (TGA) is a temperature-programmed technique. The sample is continually being weighed while passing an inert gas over it at atmospheric pressure. Thermogravimetric analysis can be done in three different ways, such as continually increasing in temperature, keeping the temperature constant or heating the sample in multiple temperature intervals. Data from the thermogravimetric analysis can be interpreted from a graphical presentation of the sample mass change vesrus the temperature or time. Genereic thermograms have multiple sections. Below 150°C, physisorbed water, low molecular weight volatile

compounds, solvents and trapped gases evolve. When the temperature reaches 250°C, the compound begins to decompose. The remaining material after TGA is non-volatile inorganic ashes and materials [56].

2.3.5 Adsorption-desorption isotherms

Adsorption-desorption isotherms is a plot of the relative pressure versus the amount of a sorbent that has been adsorbed to the surface of the sorbate. Typical sorbents are H_2 and N_2. The sorbent can bond to the sorbate in two different ways, chemical adsorption or physical adsorption. Chemical adsorption bonds by chemical bonding to the surface and form a monolayer. Physical adsorption bonds by forces such as Van der Waals, and can form a multilayer. Langmuir isotherms is an adsorption isotherm that assumes chemical bonding and monolayer [57].

BET method can be applied to physical adsorption isotherms to calculate surface area and pore size. The BET method is an extension of the Langmuir isotherm, where each layer is based on langmuir theory. The BET adsorption isotherm equation is

$$\theta = \frac{cp}{(1 - p\backslash p_0)/(p_0 + p(c-1))} \tag{2.8}$$

where c is the BET C-constant, p_0 is the vapor pressure of the adsorptive bulk liquid phase and $\vartheta$is the surface coverage, defined as

$$\theta = n_{ads}/n_m \tag{2.9}$$

where n_{ads} is the amount which is adsorbed and n_m is the entire amount which could be adsorbed. The specific surface area is calculated by rearranging equation 2.8 and plotting $\frac{1}{v[1-(p_0/p)]}$ versus $\frac{p}{p_0}$. The specific surface area, S_{BET} is calculated from following equation,

$$S_{BET} = \frac{v_m \cdot N \cdot A_x}{V} \tag{2.10}$$

where N is Avogadro number, V the molar volume of the adsorbate gas and A_x is the cross-sectional area [57].

The BJH method can be applied to adsorption desorption isotherms to estimate pore volume and size. The pore size can be measured with analysis such as t-plot or capillary condensation analysis with the Kelving equation. The Kelvin equation,

$$\ln(\frac{P}{P_0}) = \frac{2vV_1}{r_K RT} \tag{2.11}$$

is a relation between the pore critical radius and relative pressure (P/P_0) at capillary condensation. u is the surface tension of the liquid condensate, V_1 is the molar volume of the liquid condensate and r_K is the kelvin radius. By applying the Kelvin equation, the vapor pressure of the gas can be related to the Kelvin radius and a plot between the differential pore volume and pore diameter can be obtained. This plot can be used to determine the porosity [58].

CHAPTER

THREE

METHODS

This part explains the methods utilized for the preparation, characterization and activity testing of Fe/SiO_2 and red mud. The samples were prepared and characterized to investigate the impact of washing with water and HCl on catalyst deactivation due to the presence of sodium and calcium, as well as the effect of regeneration.

3.1 Preparation of sorbents

The sorbents used for this thesis are Fe/SiO_2 and red mud. Fe/SiO_2 was prepared to use as a reference state and compared with red mud. In addition, $FeCl_3/SiO_2$ was prepared to determine experimental conditions for the regeneration.

3.1.1 Fe/SiO_2

The preparation of Fe/SiO_2 was done with the incipient wetness method, with impregnation of iron nitrate, $Fe(NO_2)_3{\cdot}(H_2O)_n$ (98%), and silica as support.

In Appendix A, the calculations for the Fe and Fe_2O_3 content in Fe/SiO_2 were carried out, leading to 8.7% Fe and 12.45% Fe_2O_3. To prepare the sorbent, 19.82 g of silica was dried in an oven to remove any water content. Next, 8.16 g of iron nitrate was dissolved in distilled water in a 10 ml glass flask. While stirring regularly, droplets of the solution were added to the silica. The resulting sorbent was dried overnight in the oven and then calcined for 5 hours at 550 °C with a ramp of 3°C/min and flowing air at 75 ml/min.

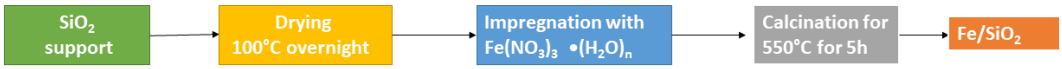

Figure 3.1.1: Block diagram for the preparation steps for Fe/SiO_2

3.1.2 Red mud

Due to the high water content in red mud, the red mud was dried for 12 hours in the oven prior to the preparation. Further, the red mud was crushed and sieved to 63-100 µm. Figure 3.1.2a shows red mud before it was synthesized and figure 3.1.2b shows the red mud after drying and sieving.

(a) Raw red mud

(b) Red mud after drying and sieving to particle size 63-100 µm.

Figure 3.1.2: Red mud before and after drying and sieving.

Further, red mud was calcined for 5 hours at 550°C before samples with different treatments were prepared. A sample of red mud was pre-reduced at 500°C and passivated for 2 hours by flowing 100 ml/min of 1% oxygen in argon at ambient temperature. Figure 3.1.3 show the red mud after the reduction and passivation.

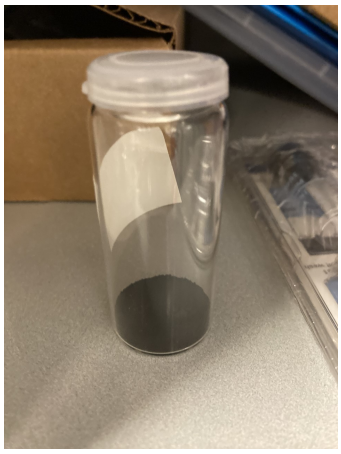

Figure 3.1.3: Red mud after calcination, reduction at 500°C and passivation

In addition, samples washed with water and HCl were also prepared. The washing with water was done two times in a buchner funnel. The water was pre-heated to 60°C and 80°C. The pH of the wash water was measured until it reached 7, indicating the removal of alkaline substances, such as sodium. The buchner funnel with red mud was dried in the oven at 100 °C overnight. The washing with HCl was carried out by mixing 5 g of red mud with diluted HCl. A 100 mL solution of 1 mol/L HCl was prepared. The solution was stirred for 2 hours before being washed with water to remove the acid. The pH of the wash water was measured until it reached 7, indicating the removal of alkaline substances. The batch was kept in the oven at 120°C overnight. Figure 3.1.5 show the preparation steps of red mud in a block diagram.

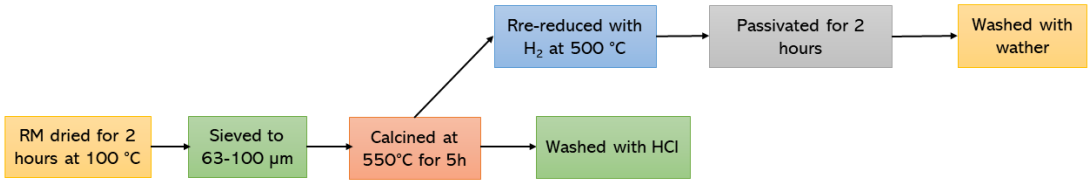

Figure 3.1.4: Block diagram for the preparation steps for red mud

Table 3.1.1 lists samples of red mud that have undergone various treatments and will be used further for experiments.

Table 3.1.1: Samples of red mud with various treatments, which have been used for the experiments.

Sorbent	Treatment
RMC	Calcined at 550°C
RMC_{water}	Calcined at 550°C and washed wit water.
RMC_{HCl}	Calcined at 550°C and washed with HCl.
RMC_{R350}	Calcined at 550° and reduced in-situ at 350°C.
RMC_{R500}	Calcined at 550°C, pre-reduced at 550°C and passivated.

3.1.3 $FeCl_3/SiO_2$

In Appendix A, the calculations for the $FeCl_3$ content in $FeCl_3/SiO_2$ were carried out, leading to 12% $FeCl_3$. $FeCl_3/SiO_2$ prepared with the incipient wetness method. Silica was dried in the oven overnight to remove the water content. 1.63 g of iron chloride (97%) from Sigma Aldrich was dissolved in distilled water until 10 ml in a glass flask. Droplets of the solution were added to 11.11 g of silica while stirring regularly. The sorbent was dried at ambient temperature for 2 days. Further, the sorbent was dried in the oven at 60 °C for 3 days. Figure 3.1.5 show a block diagram of the preparation steps of $FeCl_3/SiO_2$.

Figure 3.1.5: Block diagram for the preparation steps for $FeCl_3/SiO_2$.

3.2 Characterization of sorbent

3.2.1 TPR

Different samples of red mud Fe/SiO_2 were characterized with TPR to provide information on reduction states and hydrogen consumption.

The TPR experiment was carried out in the Altamira BenchCat TPX Analyzer, with approximately 0.1 g sorbent. The sorbent was heated to 900°C, with a ramp of 10°C/min, while flowing 7% H_2 in argon.

3.2.2 XRD

To identify the crystal phases of fresh and spent samples of Fe/SiO_2 and red mud, analysis with XRD was carried out.

Fresh and spent samples were analyzed in D8 A25 DaVinci X-ray Diffractometer. The sorbent was placed in a si-cavity 10mm holder and analyzed for 30 minutes at 10-80 ° with the step size 0.2 °/step.

3.2.3 XRF

To identify the elemental composition of fresh and spent samples of red mud and $FeCl_3/SiO_2$, analysis with XRF was performed.

The XRF analysis was carried out in the X-ray fluorescence spectrometer supermini200. During the analysis, the temperature was kept at 25 °C, the pressure was atmosphere vacuum and 10% methane in argon was provided with a flow rate of 24.8 mL/min.

3.2.4 N_2 adsorption-desorption analysis

The sorbent was evacuated for 1 hour before it was degassed with VacPrep 061 degasser overnight at 200°C. The pressure was 100mTorr. Further, the sorbent was placed in the Micrometrics Tri Start 3020 surface area and porosity analyzer to adsorb N_2. The obtained adsorption isotherm was analyzed with the BET method.

3.3 Chlorobenzene dechlorination experiments

The experiments with the different samples of Fe/SiO_2 were carried out in the gas dechlorination rig as seen in figure 3.3.1. The setup consists of 4 flowmeters, which enable the feeding of four gasses, including hydrogen, nitrogen, air, and chlorobenzene. The 4 gases are mixed before being introduced to the glass reactor from the top and travel to the bottom. subsequently, all the gases are directed to the GC, where nitrogen is measured in the TCD detector, and chlorobenzene is measured in the FID detector. Prior to the experiments, a leak test was executed.

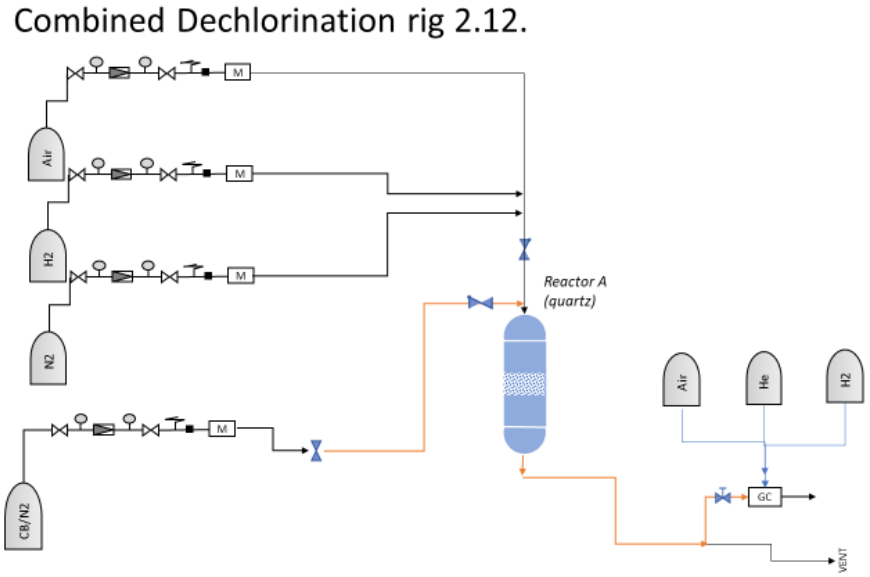

Figure 3.3.1: A schematic illustration of the dechlorination set up

The dechlorination of chlorobenzene was performed in a fixed-bed reactor (inner diameter, 12 mm) at atmospheric pressure. The sorbent was loaded in the reactor between two quartz wool plugs. The total flow in the dechlorination rig was maintained at 110 mL/min at all time. Prior to the dechlorination reaction, certain sorbents were reduced in-situ. The reduction in-situ was done by flowing 50/50 H_2 and N_2. During the dechlorination reaction, the flow was ll mL/min of chlorobenzene (0.005%) in nitrogen and 99 mL/min N_2. Certain sorbents were regenerated after the dechlorination reaction. The regeneration was done by flowing 100% air for 1 hour. The benzene content was measured using gas chromatography. Figure 3.3.2 show a schematic illustration of the experiments carried out in the gas dechlorination with chlorobenzene.

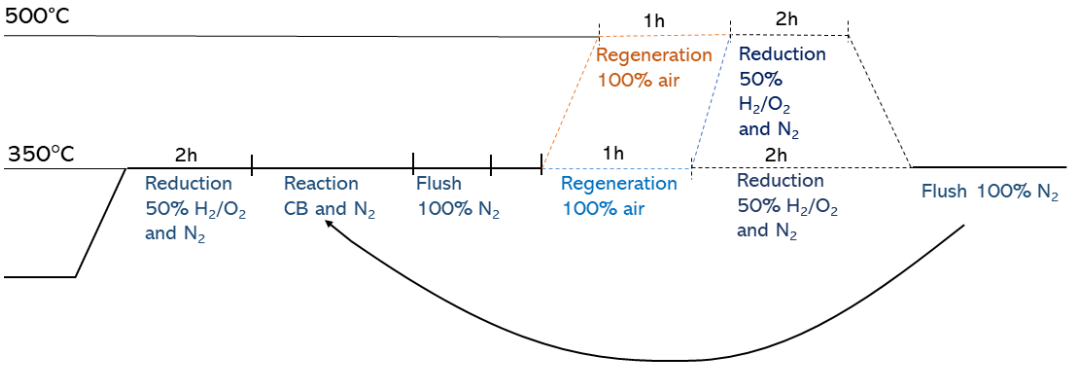

Figure 3.3.2: Schematic illustration of the experiments in the gas dechlorination with chlorobenzene.

Experiments were carried out with varying reduction temperature, regeneration temperature and space velocity. The following conditions were not changed for any experiments,

- Reduction time for 2 hours
- Reaction temperature at 350°C
- Regeneration time for 1 hour

The varied experimental conditions for the different sorbents are listed in table 3.3.1.

Table 3.3.1: Experimental conditions for the varied sorbents in the gas dechlorination of chlorobenzene

Sorbent	**Space velocity [L/(g h)]**	**Reduction temperature [°C]**	**Regeneration temperature [°C]**
Fe/SiO_2	30	350	350-450
RMC_{R500}	22-30	500	350-500
RMC	30	350	350-500
RMC_{HCl}	30	350	350

CHAPTER
FOUR

RESULTS AND DISCUSSION

This part discusses the results from the investigations with the Fe-based material, red mud, in two parts. The first part discusses the effect of washing, where samples were washed with HCl and water to eliminate sodium and calcium due to the known sintering effect. The second part discusses the effect of regeneration. In addition, various experimental conditions for the different samples have been investigated. Experiments with Fe/SiO_2 were carried out for comparison.

4.1 The effect of washing

For the first part, the effect of washing was investigated. A sample of red mud was washed with water and a sample was washed with HCl. The samples were characterized with XRD, TPR, XRF and N_2 adsorption-desorption isotherms. The activity was determined under gas dechlorination of chlorobenzene with varied experimental conditions.

4.1.1 XRD

The different phases in red mud after the various treatements were determined via XRD analysis. Figure 4.1.1 displays raw RM, RMC, RMC_{water} and RMC_{HCl}. The calcination temperature was 550°C.

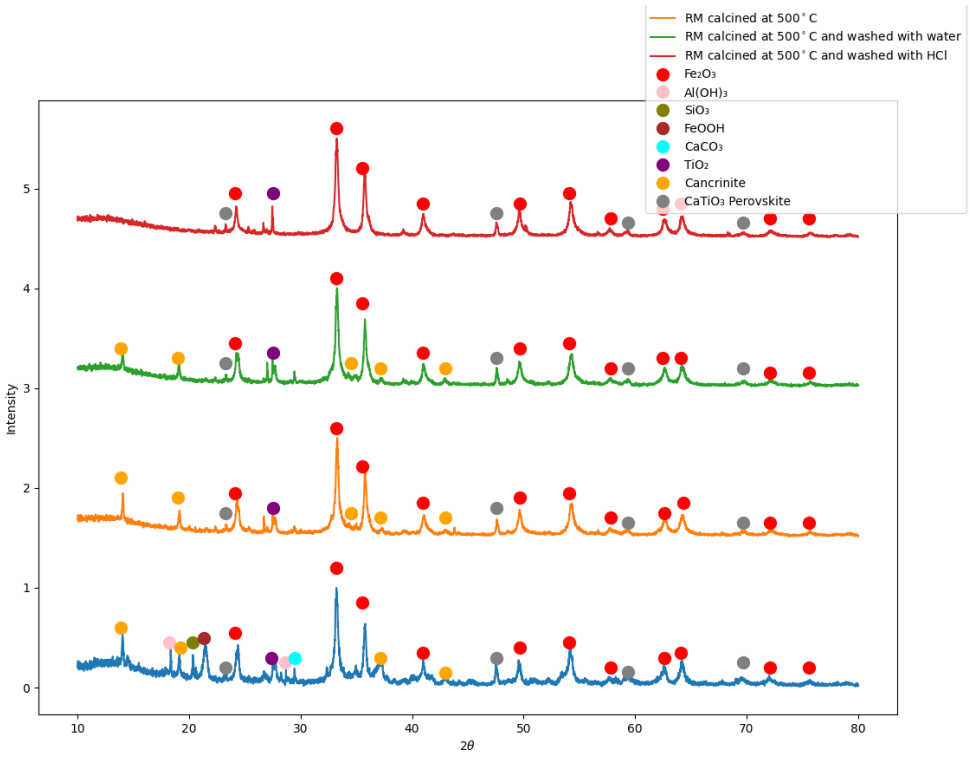

Figure 4.1.1: XRD profiles of raw RM, RMC, RMC_{water} and RMC_{HCl} (Calcined at 550°C)

The results from XRD analysis in figure 4.1.1 reveal that the raw RM comprises cancrinite, hematite (Fe_2O_3), goethite (FeOOH), silica (SiO_2), titanium dioxide (TiO_2), and perovskite ($CaTiO_3$), as expected and outlined in table 1.2.2. In the investigation by Wang et al. [43], it has been observed that calcination temperatures above 500°C have the ability to remove components such as FeOOH, $Al(OH)_3$, and SiO_2. FeOOH and $Al(OH)_3$ are decomposed into Fe_2O_3 and Al_2O_3 through oxidation, which enhances the activity of red mud in relation to iron oxide. Based on the XRD profile displayed in figure 4.1.1, it can be inferred that a temperature of 550°C removed these components.

Furthermore, it is observed in figure 4.1.1 that RMC_{water} did not exhibit any significant changes in their mineral composition. Conversely, RMC_{HCl} displayed a discernible change in composition, specifically the removal of cancrinite.

To investigate the phases in red mud after various reduction temperatures, XRD analyses were carried out for RMC_{R350}, RMC_{R500}, and Fe/SiO_2 for comparison, and is displayed in figure 4.1.2.

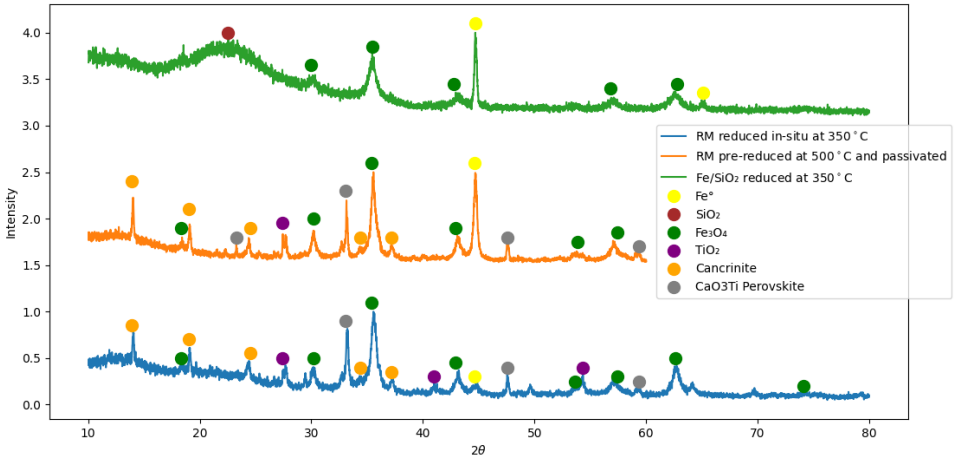

Figure 4.1.2: XRD profile of RMC_{R350}, RMC_{R500} and Fe/SiO_2 (calcined at 550°C and reduced at 350-500°C).

Figure 4.1.2 reveal that the reduction carried out at 350°C leads to the formation of a mixture of Fe_3O_4 and Fe^0 in both RMC_{R350} and Fe/SiO_2. The mixture is also detected in RMC_{R500}, where the reduction temperature is increased to 500°C. It is also observed that the Fe^0 peak for RMC_{R500} exhibits a greater sharpness compared to RMC_{R350}, indicating an increase in the crystalline structure. This could be attributed to sintering, caused by the higher temperature. However, RMC_{R350} was not passivated after the reduction and may have been oxidized when exposed to air, causing a change in the crystal size.

4.1.2 XRF

The elemental composition of RMC, RMC_{R350}, RMC_{R500}, RM_{water} and RMC_{HCl} is obtained from XRF and displayed in table 4.1.1. The samples are an average of multiple analyses.

Table 4.1.1: Elemental composition of RMC,RMC_{R350}, RMC_{R500}, RMC_{water} and RMC_{HCl} from XRF analysis

Treatment of RM	**Composition [%]**					
	Na_2O	**Al_2O_3**	**SiO_2**	**CaO**	**TiO_2**	**Fe_2O_3**
RMC	7.3	19.1	10.0	6.1	8.7	47.6
RMC_{R350}	5.4	13.2	31.3	4.7	6.9	37.0
RMC_{R500}	7.2	18.1	9.7	6.1	8.9	48.2
RMC_{water}	7.3	19.1	10.0	6.1	8.7	47.6
$RMC_{R350HCL}$	0.2	9.2	2.00	3.4	11.6	72.2

In addition to the composition displayed in table 4.1.1, traces of P_2O_5, SO_3, K_2O,V_2O_5,Cr_2O_3,Cl, MnO, ZrO_2,Nb_2O_5, Ag_2O, MgO,Co_2O_3, SO_3, CuO was also

detected.

The elemental composition depicted in table 4.1.1, is consistent with the elements depicted in table 1.2.2. The XRF analysis does not display a significant change in the elemental composition between RMC and RMC_{water}. In addition to the none significant difference revealed from the XRD analysis, this indicates that washing with water has a negligible impact. The sample washed with HCl had a remarkable effect. The elemental composition of RMC_{HCl}, including Na_2O, Al_2O_3, SiO_2 and CaO was decreased compared to RMC. This results in a higher fraction of Fe_2O_3 and TiO_2 for RMC_{HCl}, from 47.6% to 72.2% and 8.7% to 11.6% respectively. The removal of sodium is consistent with the findings by Altundoğan et al [47].

4.1.3 N_2 adsorption-desorption isotherms

The BET surface area of Fe/SiO_2, raw RM, RMC, RMC_{R500} and RM_{HCl} are obtained from N_2 adsorption-desorption isotherms and listed in table 4.1.2.

Table 4.1.2: BET surface area of $FeSiO_2$, raw RM, RMC, RMC_{R500} and RM_{HCl} from adsorption-desorption isotherms.

Sample	**BET surface area [m^2/g]**
Fe/SiO_2	451.2
RM raw	24.3
RMC	31.1
RMC_{R500}	31.0
RMC_{HCl}	41.9

In figure 4.1.2, it is observed that the BET surface area has increased after calcination at 550°C. This is consistent with the findings from Wang et al [43]. The increase in surface area is due to the removal of the impurities, which results in a higher degree of an active surface that is available for chemical reactions and further could increase the activity of the sorbent. For RMC_{HCl}, the surface area is seen to increase as well, with 24%. This is consistent with the findings by Kerry et al [45] and Paradese et al [46]. However, the increase in surface area found by Kerry et al and Paradese et al is higher. The increase in surface area may be attributed to the removal of some components including sodium, aluminium, silica and calcium, as seen from the XRF analysis presented in table 4.1.1.

In addition to the BET surface area, the BJH pore volume and area of raw RM, RMC, RMC_{R500} and RM_{HCl} were also determined from N_2 adsorption-desorption isotherms. Figure 4.1.3, 4.1.4, 4.1.5 and 4.1.6 displays the cumulative and dv/dw pore volume and area of red mud obtained from the BJH method.

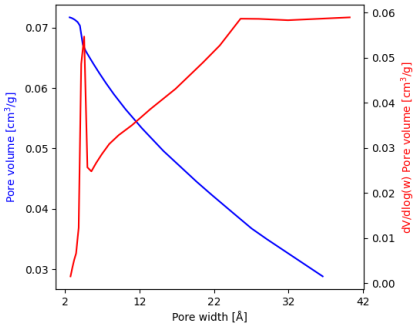

(a) Cumulative and dv/dw pore volume of raw RM.

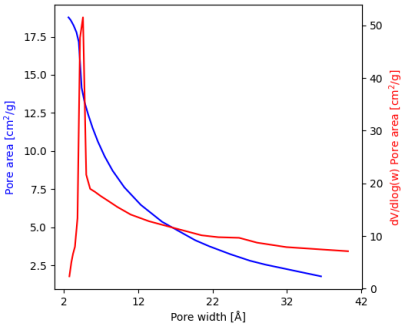

(b) Cumulative and dv/dw pore area of raw RM.

Figure 4.1.3: Cumulative and dv/dw pore volume and area of raw RM.

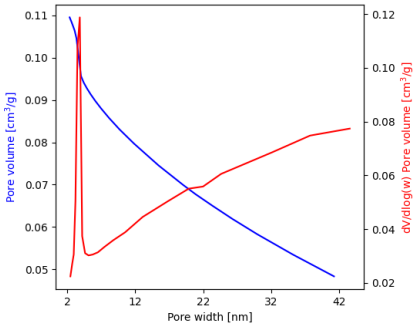

(a) Cumulative and dv/dw pore volume of RMC.

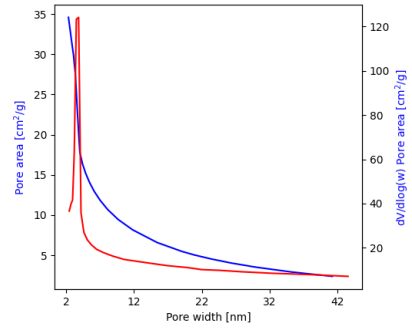

(b) Cumulative and dv/dw pore area of RMC.

Figure 4.1.4: Cumulative and dv/dw pore volume and area of RMC (calcined at 550°C).

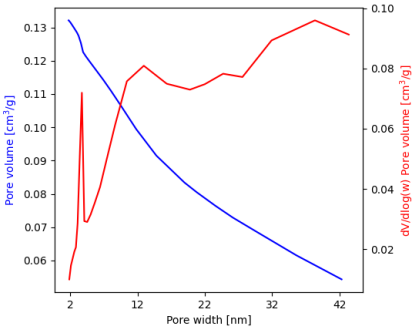

(a) Cumulative and dv/dw pore volume of RMC_{R500}.

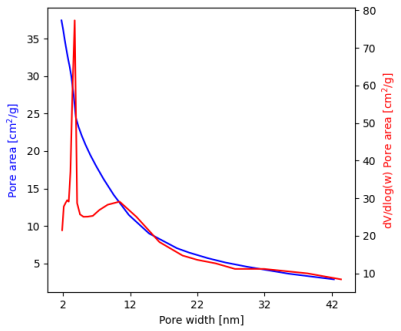

(b) Cumulative and dv/dw pore area of RMC_{R500}.

Figure 4.1.5: Cumulative and dv/dw pore volume and area of RMC_{R500} (calcined at 550°C and reduced at 500°C).

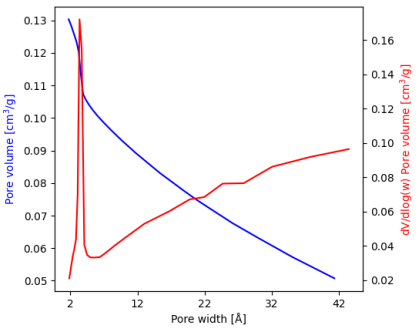

(a) Cumulative and dv/dw pore volume of RMC_{HCl}

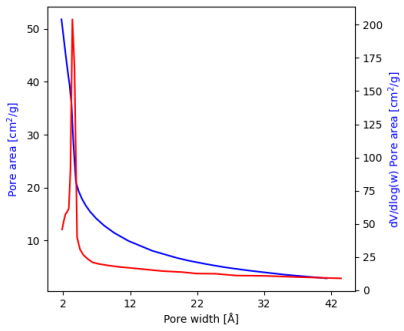

(b) Cumulative and dv/dw pore area of RMC_{HCl}.

Figure 4.1.6: Cumulative and dv/dw pore volume and area of RMC_{HCl} (calcined at 550°C and washed with HCl).

The pore volume and area obtained from the BJH method in figure 4.1.3, 4.1.4, 4.1.5 and 4.1.6 is in the mesoporous range (2-50 nm). For all the samples, it is seen that most of the area is derived from the smaller mesopores. Figure 4.1.4b shows that calcination increases the surface area by removing compounds and increasing the proportion of smaller mesopores, which enhances the overall surface area. For RMC_{R500} in figure 4.1.5a it is observed that the distribution changes to larger mesopores. This results in an additional peak observed in figure 4.1.5b, showing that more of the area is generated from bigger mesopores after reduction. However, the change in distribution before and after reduction is not particularly significant. In figure 4.1.6a it is observed that the distribution of RMC_{HCl} compared to the calcined sample in figure 4.1.6a has not changed significantly. It has been a rise in the quantity of both smaller and larger mesopores, resulting in an increase in the surface area as displayed in figure 4.1.6b and from BET, displayed in table 4.1.2.

4.1.4 TPR

Furthermore, TPR analysis was done in order to determine the reduction temperature and corresponding phases, in addition to the hydrogen consumption for Fe/SiO_2 and red mud.

Table 4.1.3 displays the theoretical values and actual values of hydrogen consumption of Fe/SiO_2. The calculations of the theoretical values of hydrogen consumption are shown in appendix 6. The actual values are determined from TPR.

Table 4.1.3: Theoretical and actual values for hydrogen consumption of Fe/SiO_2.

Sample	**Reduction**	**Theoretical value [µmol H_2/g sorbent]**	**Actual value [µmol H_2/g sorbent]**
$FeSiO_2$	$Fe_2O_3 \rightarrow Fe_3O_4$	258	255
	$Fe_3O_4 \rightarrow FeO$	518	514
	$FeO \rightarrow Fe$	1553	315
Total		2333	1085

Figure 4.1.7 displays the TPR profile of Fe/SiO_2 calcined at 550°C. The graded area corresponds to the different reduction states based on the theoretical value for hydrogen consumption seen in table 4.1.3. The darkest area corresponds to the reduction from $Fe_2O_3 \rightarrow Fe_3O_4$, the lighter area to the reduction from $Fe_3O_4 \rightarrow FeO$ and the lightest area to the reduction from $FeO \rightarrow Fe$.

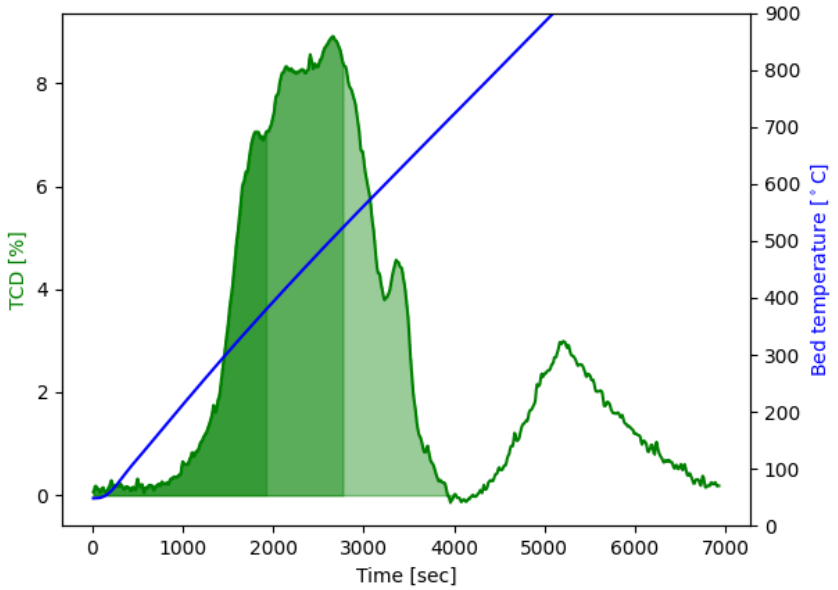

Figure 4.1.7: TPR profile of Fe/SiO_2 (calcined at 550°C).

In table 4.1.3 it is observed that the actual value of the total hydrogen consumption

differs from the theoretical value by 43%. The TPR profile of Fe/SiO_2 in figure 4.1.7 displays two noticeable peaks. The first peak indicates the reduction of iron-oxide, while the second peak indicates the reduction of iron-silica. Although table 4.1.3 implies that the sample is not fully reduced due to a higher theoretical value, figure 4.1.7 contradicts this and suggests that the excess consumption of hydrogen is caused by the formation of iron-silica phases, which also consume hydrogen. Hence, the difference between the total actual value and theoretical value in table 4.1.3, might be due to the formation of compounds of iron silica which is not reducible at these temperatures. The graded area based on the theoretical hydrogen consumption in figure 4.1.7 displays that the reduction from Fe_2O_3 to Fe_3O_4 in Fe/SiO_2 reaches a maximum uptake at 400°C. The reduction to Fe^0 reaches a maximum uptake at 450°C. From the XRD profile of Fe/SiO_2 in figure 4.1.2, it is observed that reduction at 350°C leads to a mixture of Fe_3O_4 and Fe^0, which is consistent with the observations in figure 4.1.7. In addition, it is observed that FeO is not detected from XRD in figure 4.1.2, which might be because of the instability of FeO, which quickly reduces to Fe^0. This implies that the reduction to FeO from Fe_2O_3 is comparatively more challenging than the reduction to Fe^0 from FeO.

Further, TPR of RMC, RMC_{R350}, RMC_{R500} and RMC_{HCl} were also analysed to assess the extent of the different reduction temperatures, 350°C and 500°C, and the washing with HCl. The theoretical and actual values of the hydrogen consumption are displayed in table 4.1.4. The theoretical values of RMC and RMC_{HCl} are calculated from the Fe_2O_3 content in table 4.1.1, based on the assumption that iron is the only reducible element in red mud. The calculations for the theoretical hydrogen consumption are shown in Appendix A. The actual values are determined from TPR.

Table 4.1.4: Theoretical and actual values for hydrogen consumption of RMC, RMC_{HCl}, RMC_{R350} and RMC_{R500}

Sample	**Reduction**	**Theoretical value [µmol H_2/g sorbent]**	**Actual value [µmol H_2/g sorbent]**	**Reduction degree [%]**
RMC	$Fe_2O_3 \rightarrow Fe_3O_4$	993		
	$Fe_3O_4 \rightarrow FeO$	1987		
	$FeO \rightarrow Fe$	5970		
	Total	8950	12314	
RMC_{HCl}	$Fe_2O_3 \rightarrow Fe_3O_4$	1506		
	$Fe_3O_4 \rightarrow FeO$	3010		
	$FeO \rightarrow Fe$	9030		
	Total	13546	8138	34
RMC_{R350}	Total	6969	5558	55
RMC_{R500}	Total	9052	9182	26

In the opposite of the hydrogen consumption for Fe/SiO_2 in table 4.1.3, RMC

in table 4.1.4 shows a higher actual value. In addition, these observed differences between theoretical values and actual values in table 4.1.3 and 4.1.4 can be due to the limitations of XRF as a semi-quantitative technique which may result in less precise measurements. To identify the error in XRF, the elemental composition of Fe_2O_3 has been calculated based on the hydrogen uptake from TPR in table 4.1.4 and displayed in table 4.1.5. The calculation is based on the assumption that iron is the only reducible element in red mud.

Table 4.1.5: Elemental composition of RMC,RMC_{R350}, RMC_{500} and RMC_{HCl}, based on the hydrogen consumption from TPR.

Sample	**Fe_2O_3 [%]**
RMC	66
RMC_{R350}	30
RMC_{R500}	49
RMC_{HCl}	43

From figure 4.1.5 it is evident that the elemental composition of Fe_2O_3 from XRF is subjected to certain levels of error.

The TPR profile of RMC is displayed in figure 4.1.8. The graded area corresponds to the different reduction states based on the theoretical values for the hydrogen consumption in table 4.1.4, given that iron is the only reducible element in red mud. The darkest area corresponds to the reduction from $Fe_2O_3 \rightarrow Fe_3O_4$, the lighter from $Fe_3O_4 \rightarrow FeO$ and the lightest area from $FeO \rightarrow Fe^0$.

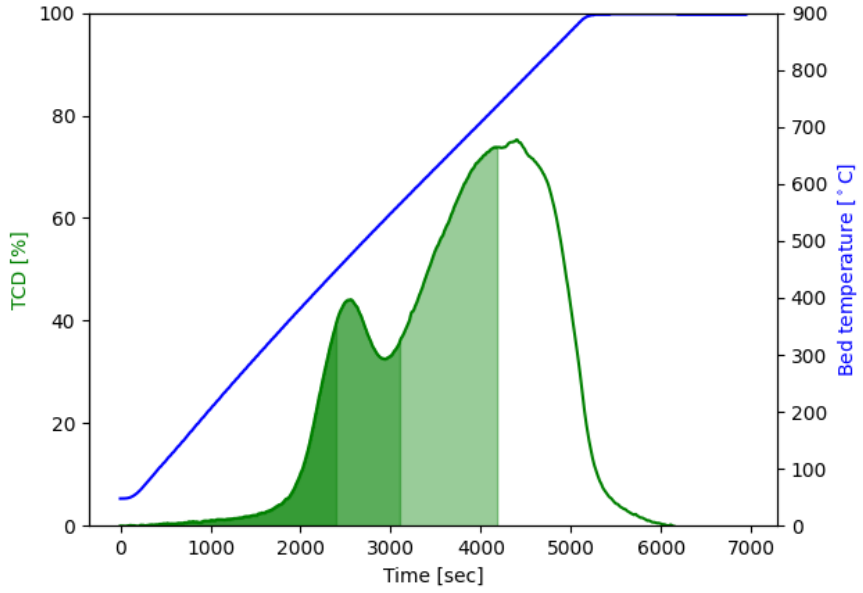

Figure 4.1.8: TPR profile of RMC (calcined at 550°C).

The TPR profile in figure 4.1.8 reveals two distinct peaks. In comparison, the TPR profile of red mud in figure 1.4.2 obtained from Ordóñez et al [44], reveals three clearly defined peaks. It is possible that this difference is due to the instability of FeO. Figure 4.1.8 displays that the maximum hydrogen consumption for the first peak is at approximately 400°C and the maximum hydrogen consumption for the second and third peaks is both around 650°C. The alignment of these peaks with those represented in 1.4.2 suggests that the reduction of Fe_3O_4 to Fe_2O_3 occurs at temperatures below 400°C, and the reduction of Fe_2O_3 to FeO and Fe occurs at temperatures below 650°C. This is also consistent with the findings from the XRD profiles in figure 4.1.2 of RMC_{R350} and RMC_{R500}, which contain of a mixture of Fe_3O_4 and Fe^0. However, it is noticed in table 4.1.4 and in figure 4.1.8 that the actual value is higher than the theoretical value. This indicates that iron is not the only reducible element in red mud.

Figure 4.1.9 displays the TPR profile of RMC_{R350}(4.1.9a), RMC_{R500}(4.1.9b)and RMC_{HCl}(4.1.9c).

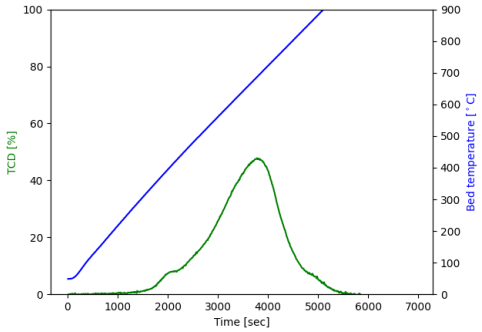

(a) TPR profile of RMC_{R350} (Calcined at 550°C and reduced at 350°C).

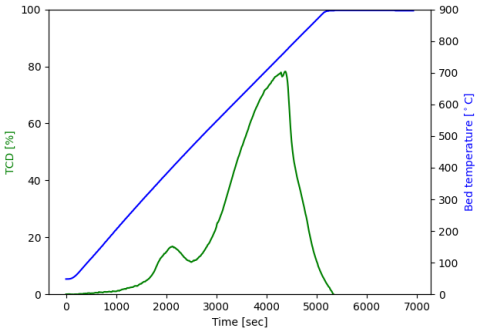

(b) TPR profile of RMC_{R500} (Calcined at 550°C and reduced at 500°C).

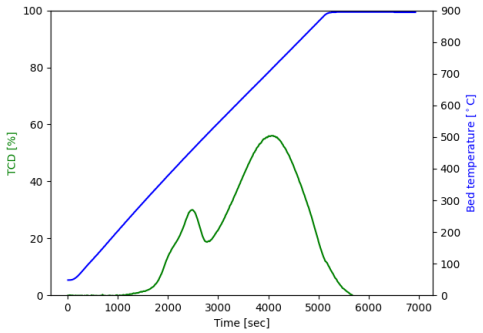

(c) TPR profile of RMC_{HCl} (Calcined at 550°C and treated with HCl).

Figure 4.1.9: TPR profile of RMC_{R350}, RMC_{R500} and RMC_{HCl} (Calcined at 550°C, reduced at 350-500°C and treated with HCl).

From table 4.1.4, it is observed that RMC_{R350} has a higher reduction degree compared to RMC_{R500}. The TPR of RMC_{R500} took place 1-2 months after the XRD analysis. This time lapse could have resulted in the oxidation of the sample, despite its passivation, leading to a lower reduction degree. Upon comparing RMC with RMC_{500} and RMC_{350} in figure 4.1.9, it is evident that RMC_{500} has undergone

a higher level of oxidation, although it is likely that RMC_{350} has oxidized as well. This can be attributed to the more comparable profiles of RMC_{500} and RMC. Due to the higher degree of Fe^0 in RMC_{R500} observed from XRD analysis in figure 4.1.2, this indicates that Fe^0 is more easily to oxidize.

RMC_{HCl} in figure 4.1.9c displays a similar profile as with RMC in figure 4.1.8. However, in table 4.1.4 it can be observed that the hydrogen consumption for RMC_{HCl} demonstrates an opposite trend to RMC's theoretical and actual values. In addition, it is noteworthy that in table 4.1.5 the elemental composition of Fe_2O_3, which is based on the hydrogen consumption from TPR, is significantly lower compared to the composition from XRF in table 4.1.1. This can indicate that the washing with HCl formates species that are not reducible under these conditions and a higher temperature could be required. It is known that when titanium is in contact with metals, titanium develops a strong interaction and covers its surface, which makes it more difficult to reduce and requires higher temperatures [59].

4.1.5 Gas dechlorination

To test the activity with the effect of washing and different reduction temperatures, experiments with gas dechlorination were carried out for RMC, RMC_{R500} and RMC_{HCl} under the same conditions. For comparison, an experiment with Fe/SiO_2 was carried out.

Figure 4.1.10 displays the conversion (4.1.10a) and the capacity (4.1.10b) of chlorobenzene with time and RMC, RMC_{500}, RMC_{HCl} and Fe/SiO_2 as sorbents. The sorbents were calcined at 550°C and reduced in-situ at 350°C for 2 hours or prereduced at 500°C. The reaction temperature was 350°C. The space velocity was 30 L/(g h). RMC_{500} was reduced in-situ at 350°C to remove the passivation layer. Two identical experiments with Fe/SiO_2 are carried out to validate the reproducibility.

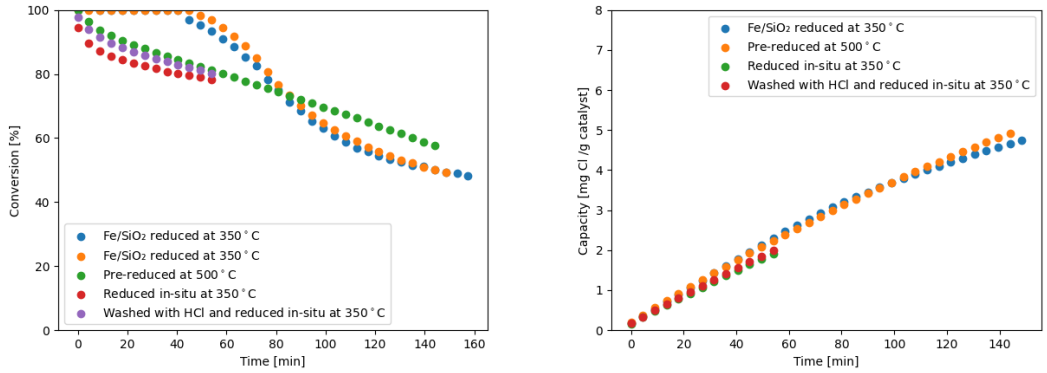

(a) Conversion of chlorobenzene with time and with RMC, RMC_{R500}, RMC_{HCl} and Fe/SiO_2 as sorbent.

(b) Capacity of chlorobenzene with time and with RMC, RMC_{R500}, RMC_{HCl} and Fe/SiO_2 as sorbent.

Figure 4.1.10: Conversion and capacity of chlorobenzene with time and RMC, RMC_{R500}, RMC_{HCl} and Fe/SiO_2 as sorbent (calcined at 550°C, reduced at 350-500°C for 2 hours, reaction temperature at 350°C and space velocity of 30 L/(g h).

In figure 4.1.10a it is observed that the conversion for Fe/SiO_2 is 100% for the first 40 minutes on the stream before the breakthrough curve is reached. Further, the conversion decreases to 60% before it reaches greater stability. Figure 4.1.10b indicates that the total capacity for Fe/SiO_2 is approximately 5 mg Cl/g sorbent.

Compared to Fe/SiO_2, it is observed in figure 4.1.10a that the conversion of RMC is lower. However, figure 4.1.10b displays that Fe/SiO_2 and RMC reach the same capacity. This indicates that the reaction in RMC is slower. Furthermore, this supports the idea that iron is not the only active element present in red mud. If iron were the only active element, the conversion rate would be closer to that of Fe/SiO_2, or potentially even higher, due to the higher iron content in red mud.

From figure 4.1.10 it can be observed that the various reduction temperatures do not have a significant impact on the activity. As previously stated from TPR analyses, RMC_{R500} had a higher degree of oxidation due to time. However, this experiment was carried out closer to the passivation, hence it is expected that the degree of oxidation for RMC_{R500} is lower for the sample carried out in 4.1.10, compared to TPR. Due to the higher degree of Fe^0 in RMC_{R500} and that Fe^0 might be easier to oxidize, this indicates that RMC and RMC_{R500} had a more similar reduction state in prior to the experiments. Since both the samples were reduced at 350°C prior to the reaction, this can explain the negotiable low difference between RMC and RMC_{R500} in figure 4.1.10. Furthermore, this can also indicate that red mud is not as sensitive to the reduction of iron and that other elements in red mud contribute to the dechlorination reaction.

From figure 4.1.10a, it is also observed that RMC_{HCl} did not exhibit a significant difference in activity either. This finding contrast with several studies [48][46], which suggests that washing with HCl can enhance the activity because sodium

and calcium contribute to sintering. However, the calcium content is only reduced by approximately 50%, which means that there is still some calcium present in the sample that could contribute to sintering. In addition, it has been observed that the surface area in the related findings has undergone a more significant increase compared to the reported surface area in table 4.1.2. A greater surface area can contribute to greater active sites available for the adsorption of chlorine. Due to the near-complete removal of sodium, as seen in table 4.1.1, figure 4.1.10 indicates that the removal of sodium was inefficient. The negotiable difference between RMC and RMC_{HCl} can be due to the formation of nonreducible species, as already mentioned. Even though the iron content as seen in table 4.1.1 is 72.2%, not all the iron is active due to nonreducible species under these conditions, leading to an activity level similar to RMC.

4.2 The effect of regenaration

For the second part, the effect of regeneration was investigated for the non-washed and washed samples of red mud. The activity was determined under gas dechlorination with varied experimental conditions. In order to determine regeneration conditions, analysis of $FeCl_3/SiO_2$ with XRF and TGA was done.

4.2.1 XRF

Analyses with XRF were done to validate the elemental composition of $FeCl_3/SiO_2$. The results are displayed in table 4.2.1.

Table 4.2.1: Results from XRF of $FeCl_3/SiO_2$

Sample	**SiO_2**	**Cl**	**Fe_2O_3**	**Trace of**
$FeCl_3/SiO_2$	87.7%	3.2%	8.0 %	Al_2O_3,SO_3 K_2O,CaO,Cr_2O_3,Rh_2O_3

Table 4.2.1 validates the chlorine content in the sample preparation, and it is observed that it is 3.2%. It can also be observed that the Fe_2O_3 content is 8.0%.

4.2.2 TGA

TGA has been employed to ascertain the conditions for regeneration in relation to the mass variation caused by the reduction in chlorine content resulting from the addition of air as seen in equation 2.5.

Figure 4.2.1 displays the TGA profile of $FeCl_3/SiO_2$. The red graph corresponds to the temperature, the blue graph to the mass loss and the green graph to the DSC signal.

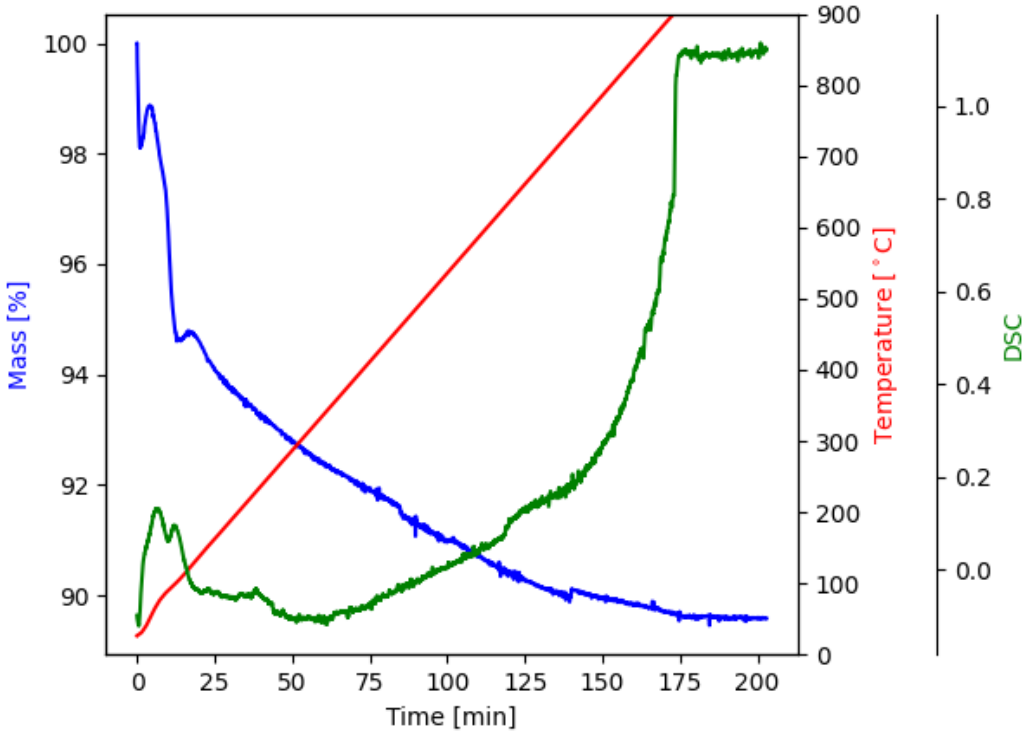

Figure 4.2.1: TGA profile of $FeCl_3/SiO_2$

Figure 4.2.1 displays that the most significant drop in the mass occurs at temperatures up to approximately 350°C. The reduction in mass continues to decrease until the temperature reaches 700°C, and the mass becomes relatively stable. It takes around 2 hours to reach this point. Additionally, the mass for the first 20 minutes until reaches 100°C is due to the presence of water.

From an industrial perspective, it is advantageous to regenerate at the same temperature as the reaction temperature to minimize energy demand and expenses, which is around 350°C. In addition, as previously stated, there is no significant difference between RMC_{350} and RMC_{500}, thereby favoring 350°C as the reduction temperature as well. Furthermore, temperatures exceeding 700°C can potentially cause sintering, as suggested by Wang et al. [43].

4.2.3 Gas dechlorination

Due to the TGA analysis and an industrial point of view, the activity in terms of the effect of regeneration was investigated with regeneration temperatures of 350°C. In addition, experiments with regeneration at 500°C were carried out as a reference.

Experiments with Fe/SiO_2 were carried out to compare with red mud. Figure

4.2.2 show the conversion (4.2.2a) and capacity (4.2.2b) of chlorobenzene with time with and Fe/SiO_2 as sorbent. The sorbent is calcined at 550°C, reduced in-situ at 350°C for 2 hours. The reaction temperature was 350°C and the regeneration temperature was 350-450°C. The space velocity was 30 L/(g h).

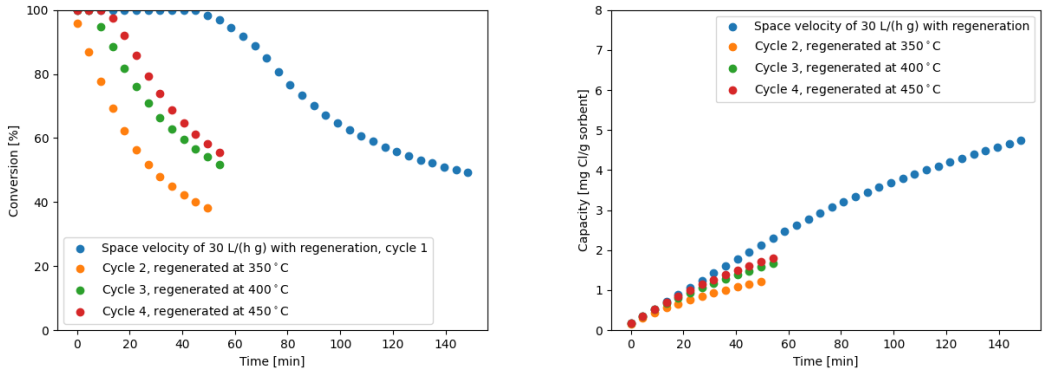

(a) Conversion of chlorobenzene with time and Fe/SiO_2 as sorbent.

(b) Capacity of chlorobenzene with time and Fe/SiO_2 as sorbent.

Figure 4.2.2: Conversion of chlorobenzene with time and Fe/SiO_2 as sorbent (calcined at 550°C, reduced at 350°C for 2 hours, reaction at 350°C, regeneration at 350-450°C and the space velocity was 30 L/(g h)).

For all the cycles regenerated in figure 4.2.2a, it is observed that the initial conversion is 100%. However, the first cycle after regeneration at 350° in figure 4.2.2a illustrates a substantial reduction and drops 64% in conversion. Further, the activity in cycles 2 to 4 shows a greater conversion, due to an increase in regeneration temperature. The regeneration yields greater stability when the temperature is increased from 400°C to 450°C. This implies that higher regeneration temperature for Fe/SiO_2 promotes recovery of a greater amount of sorbent upon airflow. In comparison with the investigation by Lingaiah et al[42], the regenerated cycles in figure 4.2.2a illustrate an initial higher conversion. In figure 4.2.2a, the conversion reaches 100% after regeneration, whereas Lingaiah et al's experiments resulted in only an 80% conversion. The investigation carried out by Lingaiah et al was performed with flowing He during regeneration. Although the experiment is not exactly the same, this could indicate that red mud regenerates better when exposed to air. In figure 4.2.2b it can be observed that the capacity reaches 2 mg chlorine/g sorbent when the temperature is raised above 400°C. The capacity curve for the first cycle exhibits a faster increase due to the higher conversion, resulting in earlier attainment of full capacity. However, when the regeneration temperature is increased to 400°, the conversion in figure 4.2.2a is relatively low indicating that regeneration of Fe/SiO_2 under these conditions is not efficient.

Furthermore, experiments to evaluate the impact of regeneration using red mud as a sorbent was carried out. Figure 4.2.3 displays the conversion (4.2.3) and capacity (4.2.3b) of chlorobenzene with time and RMC as sorbent. The sorbent was calcined at 550°C and reduced in-situ at 350°C for 2 hours. The reaction tem-

perature was 350°C and the regeneration temperature was 350-500°C. The space velocity was 30 L/(g h).

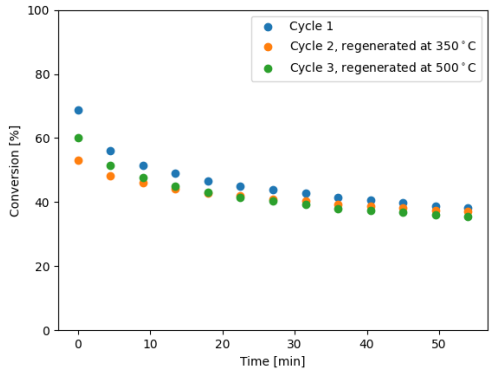

(a) Conversion of chlorobenzene with time and RMC as sorbent.

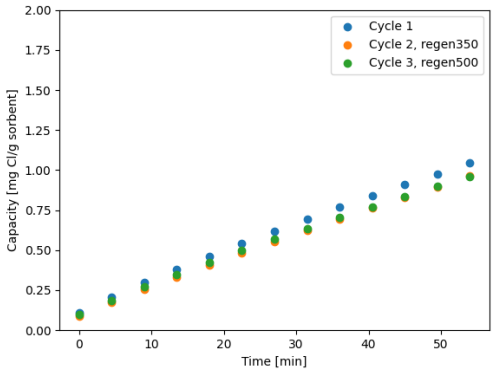

(b) Capacity of chlorobenzene with time and RMC as sorbent.

Figure 4.2.3: Conversion and capacity of chlorobenzene with time and RMC as a sorbent (calcined at 550°C, reduced at 350°C for 2 hours, regeneration temperature from 350-500°C and the space velocity was 30 L/(g h)).

From figure 4.2.3b it can be observed that the activity after regenerating at 350°C and 500°C does not yield any significant difference. In addition, both cycles after regneration, regenerate most of their activity. The capacity in figure 4.2.3b illustrates that the capacity reaches 1 mg chlorine/g sorbent.

However, by comparing the conversion in the first cycle in figure 4.2.3 with the conversion carried out under the same conditions in figure 4.1.10, it is evident that the conversion in figure 4.2.3 is significantly lower. This indicates that red mud is not reproducible under these circumstances. As seen in table 1.2.2, red mud contains of a complex composition of different elements. As already suggested, it is possible that other elements contribute to the dechlorination reaction, such as sodium, calcium and titanium. As suggested [48][46], sodium and calcium-based materials in red mud can contribute to poor activity due to sintering. Moreover, other investigations suggest that sodium and calcium-based materials are effective sorbent materials during dechlorination[40][28][37]. From the XRD profile in figure 4.1.1, it is observed that calcined red mud contains cancrinite ($Na_6Ca_2[(CO_3)_2|Al_6Si_6O_{24}]\cdot_2H_2O$) and perovskite ($CaTiO_2$) as sodium and calcium based material. Furthermore, in figure 4.1.10, it was seen that the removal of sodium and partly calcium was inefficient towards the conversion. However, there is still a presence of calcium in the sample, which could potentially impact the reaction. Detection through XRD is only possible with crystalline phases, resulting in a possibility that other calcium-based materials which are not detected can exist in red mud as well. The operating temperature is a crucial factor to be taken into account as well and can have a significant effect on the activity of the various materials in red mud.

In addition, red mud is not completely homogenous and uniform resulting in an

uneven dispersion through the entire material. The combinations of different elements which can contribute to and inhibit the dechlorination reaction with uneven dispersion, may lead to the non-reproducibility observed in red mud from figure 4.1.10 and 4.2.3. The degree of dispersion for red mud can also influence the activity, a high dispersion facilitates a greater proportion of the catalyst surface area to come into contact with reactants. Furthermore, the nonhomogenous character of red mud can result in different interactions between metals, leading to different reduction states and levels of activity.

Despite the challenges with red mud in activity, further investigations with regeneration temperature at 350°C were carried out due to the significantly low difference between 350°C and 500°C observed in figure 4.2.3. Figure 4.2.4 displays the conversion (4.2.4a) and capacity (4.2.4b) of chlorobenzene with time and RMC as sorbent. The sorbent was calcined at 550°C and reduced in-situ at 350°C for 2 hours. The reaction temperature and the regeneration temperature was 350°C. The space velocity was 30 L/(g h).

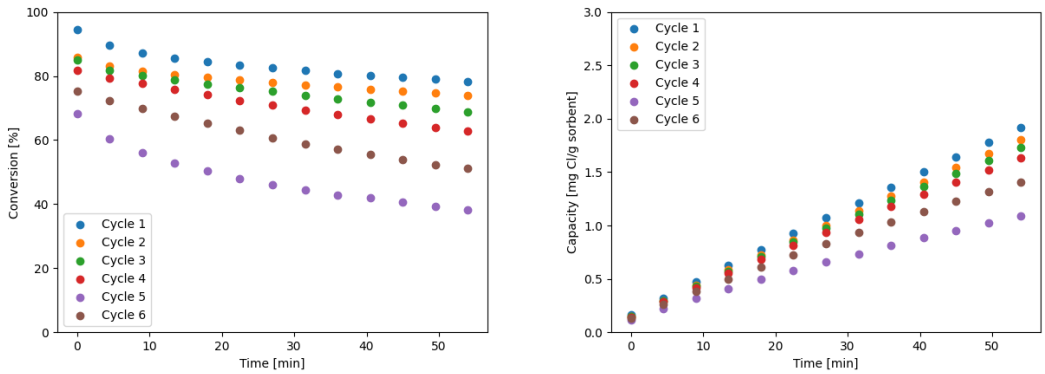

(a) Conversion of chlorobenzene with time and RMC as sorbent.

(b) Capacity of chlorobenzene with time and RMC as sorbent.

Figure 4.2.4: Conversion and capacity of chlorobenzene with time and RMC as sorbent (calcined at 550°C, reduced at 350°C for 2 hours, reaction temperature at 350°C and regeneration temperature at 350°C. The space velocity was 30 L/(g h)).

In figure 4.2.4a it can be observed that the activity of the initial three cycles regenerated most of its activity in each subsequent cycle. After the fourth cycle, there is a noticeable decrease in activity which subsequently increases after the fifth cycle. This implies that it is some reactivation. A mechanism suggested by Lingaiah et al [42] in addition to other elements in red mud, such as titanium, can clarify the behavior of red mud in the observed activity seen in figure 4.2.4a. Lingaiah et al suggest that iron oxide initially acts as a catalyst and produces HCl. Further, the HCl is adsorbed by the iron oxide, which is evidenced by the gradual decrease in conversion with time and the gradual increase in capacity. The adsorption process results in the formation of iron chloride, which once again serves as a catalyst and this is evidenced by the stabilization of conversion observed in figure 4.2.4a. When

titanium, carbon, and HCl are in contact, the formation of $TiCl_3$ or $TiCl_4$ could occur. The compounds $TiCl_3$ and $TiCl_4$ are highly unstable and susceptible to vaporization. This can cause sudden loss of chlorine and causes the reactivation observed in figure 4.2.4a[59]. It is possible that the various activities observed in regenerated RMC are a result of its nonhomogeneous character, leading to varying reduction states and levels of activity.

In addition, the TGA profile depicted in figure 4.2.1, illustrates that the elimination of chlorine is not fully completed until after around 2 hours. This indicates that one hour for regeneration is insufficient for complete regeneration. After 1 hour on the stream, the capacity varies between 1 and 2 mg chlorine/g sorbent for the cycles in figure 4.2.4.

In comparison with Fe/SiO_2 in figure 4.2.2a, it is evident that Fe/SiO_2 achieves a 40% conversion after 40 minutes in the first cycle of regeneration. However, RMC requires five regeneration cycles to reach the same conversion, as shown in figure 4.2.4a. This suggests that red mud has a greater regeneration capability compared to Fe/SiO_2 and that the various components within RMC aid in the process of regeneration.

To enhance the discovery of sodium and calcium-based materials within the regeneration effect, investigations with the regeneration of RMC_{HCl} have been carried out. Figure 4.2.5 displays the conversion (4.2.5a) and capacity (4.2.5b) of chlorobenzene with time and RMC_{HCl}, as sorbent. The sorbent is calcined at 550°C, reduced in-situ at 350°C for 2 hours. The reaction and regeneration temperature was 350°C. The space velocity was 30 L/(g h).

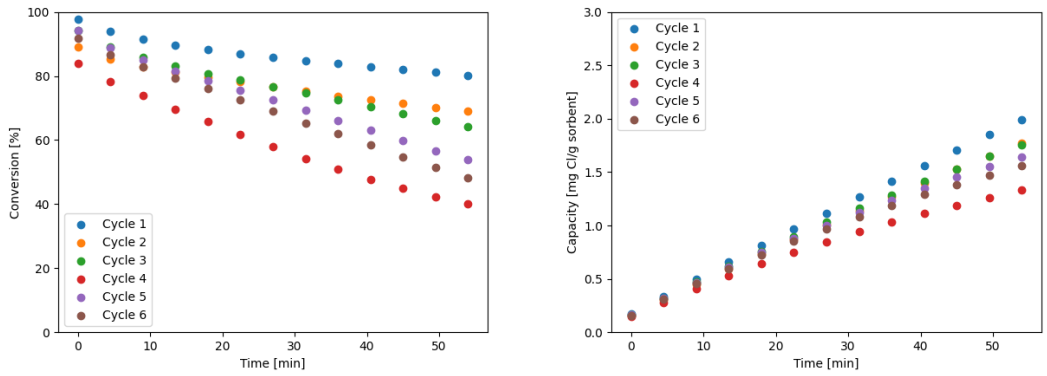

(a) Conversion of chlorobenzene with time and RMC_{HCl} as sorbent.

(b) Capacity of chlorobenzene with time and RMC_{HCl} as sorbent.

Figure 4.2.5: Conversion and capacity of chlorobenzene with time and RMC_{HCl} as sorbent (calcined at 550°C, reduction temperature at 350°C for 2 hours, reaction temperature at 350°C and regeneration temperature at 350°C. The space velocity was 30 L/(g h)).

In figure 4.2.5a, it can be observed that the initial two subsequent cycles have regenerated most of its activity. Following the third cycle of regeneration, there is a

noticeable decrease in activity before it reactivates again. After the reactivity, the activity in the subsequent cycles is further reduced. Compared to the reactivity observed in the 6th cycle in figure 4.2.4a, the reactivity in figure 4.2.5a is observed at an earlier point, specifically after the 4th cycle. The observed reactivity and behaviour in figure 4.2.5a can be explained with the same mechanism suggested by Lingaiah et al [42] and the presence of titanium. As observed in table 4.1.1, the washing with HCl did not remove titanium. In addition, other elements could contribute to the detchlorination reaction, as already suggested. Furthermore, by comparing the observations in figure 4.2.4a and in figure 4.2.5a, a significant difference is not revealed, leading to the indication that removal of sodium and partly calcium was not efficient for regeneration under the given conditions. Although the reactivity is observed at an earlier point in figure 4.2.5a, this can be a coincidence related to the challenges with the reproducibility of red mud.

It is observed that the capacity for RMC_{HCl} in figure 4.2.5b ranges between 1 and 2 mg chlorin/g sorbent after 1 hour on the stream, similar to the observations made for RMC in figure 4.2.4b.

Although it was not observed a significant difference in the activity for the different regenerations temperatures, 350°C and 500°C in figure 4.2.3, an experiment with RMC_{R500} was carried out to study the effect of reduction through regeneration. Figure 4.2.6 display the conversion (4.2.6a) and the capacity (4.2.6b) for chlorobenzene with time and RMC_{R500} as sorbent. The sorbent is calcined at 550°C and pre-reduced at 500°C for 2 hours. The reaction temperature is 350°C and the regeneration temperature was 350-500°C. The space velocity was 22 L/(g h). RMC_{R500} is reduced in-situ at 350°C in prior to the first cycle to remove the passivation layer.

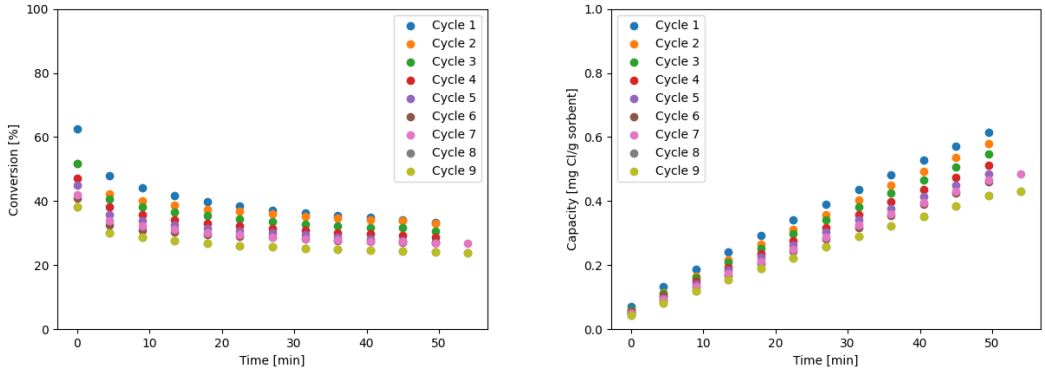

(a) Conversion of chlorobenzene with time and RMC_{R500} as sorbent.

(b) Capacity of chlorobenzene with time and RMC_{R500} as sorbent.

Figure 4.2.6: Conversion and capacity of chlorobenzene with time and RMC_{R500} as sorbent (calcined at 550°C, reduced at 500°C for 2 hours, regeneration temperature at 350-500°C. The space velocity was 22 L/(g h)).

In figure 4.2.6a it is observed that the activity has decreased significantly com-

pared to the sample in figure 4.1.10a, carried out under the same conditions. As already mentioned, this could be due to the non-reproducibility of red mud. It is worth noting that the experiment in figure 4.2.6 was conducted at a later time, suggesting that the decrease in activity may be due to oxidation over time despite the sample being passivated as previously discussed. The activity in figure 4.2.6 is similar to the activity observed in figure 4.2.3, although the reduction temperature is different. This can be due to the oxidation, despite passivation, and the initial reduction in-situ at 350°C or that red mud is not as sensitive to the reduction of iron, and other elements could contribute to the dechlorination reaction, as earlier discussed.

It is worth noticing that the activity for the subsequent cycles in figure 4.2.6a has a lower decrease compared to the experiments in figure 4.2.4a and 4.2.5a which have an initial higher conversion. It seems that higher levels of chlorine adsorption result in poorer regeneration, based on the assumption that the different reduction temperature is not significant. For the capacity in figure 4.2.6b it appears that the capacity is about 0.6 mg chlorine/g sorbent after 1 hour. On the other hand, the capacity in figure 4.2.4b shows a slightly higher capacity after one hour. This is expected due to the higher space velocity, and the total capacity will be equivalent if the reaction was carried out for a longer time.

4.2.4 XRF

To determine the chlorine composition after the dechlorination reaction for the different samples, XRF analysis was employed. The results from XRF for RMC and RMC_{HCl} are displayed in table 4.2.2. The spent samples were reduced at 350°C. The reaction temperature was 350°C and the regeneration temperature was 350°C for 6 cycles. The space velocity was 30 L/(g h).

Table 4.2.2: The chlorine composition of RMC and RMC_{HCl} before and after the dechlorination reaction, obtained from XRF analysis (Calcined at 550°C, reduction, reaction and regeneration temperature was 350°C. The space velocity was 30 L/(g h)).

Sample	**Cl [%]**
RMC	0.1
RMC *spent*	0.7
RMC_{HCl}	-
RMC_{HCl} *spent*	0.3

In addition to the composition displayed in table 4.2.2, traces of P_2O_5,SO_3,Cl, K_2O,V_2O_5,Cr_2O_3,MnO,ZrO_2,Nb_2O_5,Ag_2O,MgO,Co_2O_3,SO_3,CuO was also detected from XRF of red mud.

It can be observed in table 4.2.2 that the content of chlorine has increased after the reaction, which is expected due to the adsorption. From figure 4.2.3b and

figure 4.2.5b it can be observed that the capacity reaches 2 mg/g sorbent for both RMC and RMC_{HCl}. This corresponds to 0.2%, which is lower compared to the chlorine content obtained from XRF in table 4.1.1. This indicates that the chlorine has been adsorbed to its maximum capacity. The higher value observed from XRF could be due to accumulation because of regeneration.

4.2.4.1 XRD

The samples was analysed with XRD after the reactions to determine the composition and calculate the crystal size.

Table 4.2.3 displays the calculated crystal sizes for RMC, RMC_{HCl} and RMC_{500} from XRD before and after the reaction. The sorbent was calcined at 550°C, reduced at 350-500°C, regenerated at 350-500° and reaction temperature at 350°C. The space velocity was 30 L/(g h). RMC_{R500} was reduced in-situ at 350°C prior to the first cycle to remove the passivation layer. However, the calculations for crystal size in XRD can be restricted due to overlaps between phases.

Table 4.2.3: The calculated crystal sizes for RMC_{R350}, RMC, RMC_{R500} and RMC_{HCl} from XRD before and after the reaction (calcined at 550°C, reduced at 350-500°C, regenerated at 350-500° and reaction temperature at 350°C. The space velocity was 30 L/(g h)).

Sample	**Fe_3O_4 [nm]**	**Fe^0[nm]**
RMC_{R350}	17	37
RMC, spent	20	35
RMC_{HCl}, spent	20	35
RMC_{R500}	21	27
RMC_{R500}, spent	18	26

Figure 4.2.7 displays the XRD of RMC and RMC_{HCl} after reaction with regeneration and compared to RMC_{R350}. The sorbent was calcined at 550°C and reduced at 350°C for 2 hours. The reaction temperature was 350°C and the regeneration temperature was 350°C. The space velocity was 30 L/(g h).

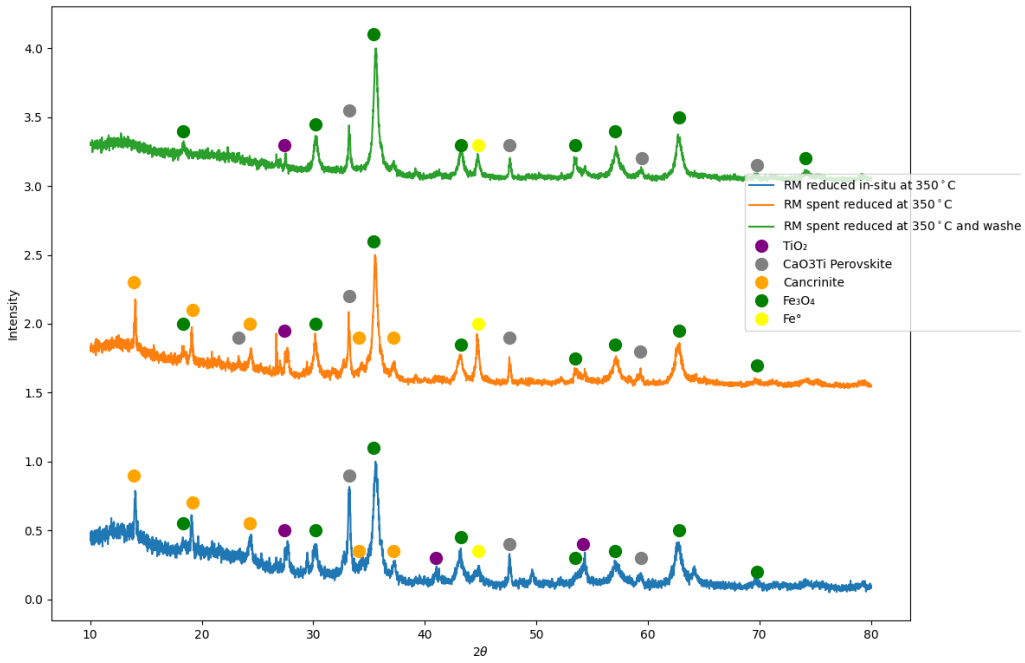

Figure 4.2.7: XRD profile of RMC and RMC_{HCl} after reaction with regeneration and compared to RMC_{R350} (Calcined at 550°C, reduced at 350°C for 2 hours, reaction temperature at 350°C, regeneration temperature at 350°C and the space velocity was 30 L/(g h)).

Figure 4.2.7 displays that the composition after the reaction remains a mixture of Fe_3O_4 and Fe^0. However, RMC_{R350} was not passivated after the reduction, leading to a possible higher oxidation state in the XRD. An XRD analysis with RMC_{HCl} was not carried out, but assuming it is similar to the XRD analysis of RMC, without the presence of cancrinite. It can be observed that the Fe^0 peak exhibits a greater sharpness after the reaction for RMC and RMC_{HCl}. This could be attributed to sintering during the reaction.

From table 4.2.3 it is observed that the crystal size of Fe^0 has decreased for RMC_{R350} and RMC_{HCl} after the reaction. The decrease in crystal size of Fe^0 could be the result of $FeCl_3$ covering the Fe particles and causing them to melt into smaller particles due to the low melting point for $FeCl_3$. However, it is unclear if the dechlorination reaction produces $FeCl_2$ of $FeCl_3$. Furthermore, this may result in partial regeneration, which could partially explain why the sample depicted in figure 4.2.4a has not fully regenerated. However, the decrease in crystal size is quite minimal. There is no significant difference in the size of Fe_3O_4 between RMC_{350} and RMC_{HCl} after the reaction. This is in consistent with the similar activity displayed in figure 4.2.4a and figure 4.2.5a.

Figure 4.2.8 displays RMC_{R500} before and after reaction with regeneration. The sorbent was calcined at 550°C and pre-reduced at 500°C for 2 hours and re-

duced in-situ at 500° after regeneration. The reaction temperature was 350°C and the regeneration temperature was 350-500°C. The space velocity was 22 L/(g h). RMC_{500} was reduced in-situ at 350°C prior to the first cycle to remove the passivation layer.

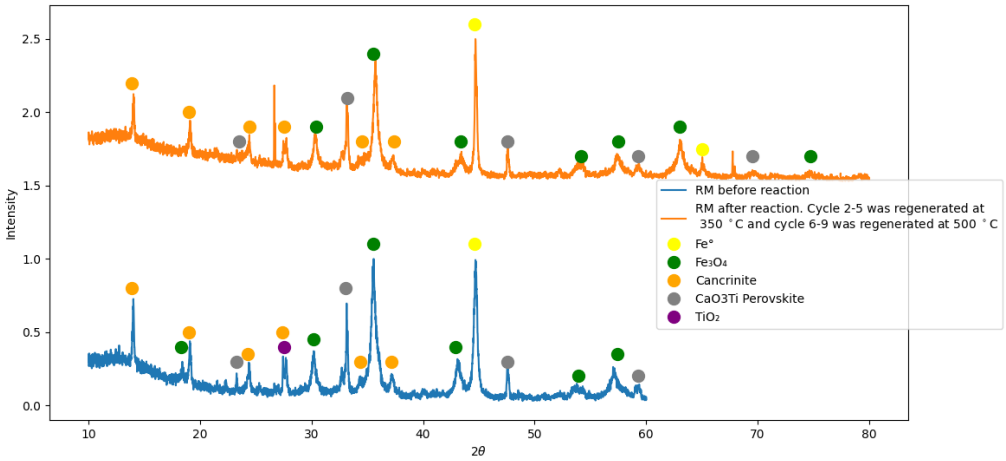

Figure 4.2.8: XRD profile of RMC_{R500} (Calcined at 550°C, reduced at 500°C for 2 hours, reaction temperature at 350°C, regeneration temperature at 350-500°C and space velocity was 22 L/(g h)).

Similar to the XRD profiles in figure 4.2.7, the composition after the reaction for RMC_{R500} in figure 4.2.8 is a mixture of Fe_3O_4 and Fe^0 as well and the composition before and after the reaction is quite similar. From table 4.2.3 it can be observed that the crystal sizes of Fe_2O_3 and Fe^0 are quite similar before and after the reaction as well.

4.2.5 N adsorption-desorption isotherms

The BET surface area of RMC_{R500} was measured with N_2 adsorption-desorption isotherms before and after the reaction, and is displayed in table 4.2.4. The sorbent was calcined at 550°C and pre-reduced at 500°C for 2 hours and reduced in-situ at 500° after regeneration. The reaction temperature was 350°C and the regeneration temperature was 350-500°C. The space velocity was 22 L/(g h). RMC_{500} was reduced in-situ at 350°C prior to the first cycle to remove the passivation layer.

Table 4.2.4: BET surface area for RMC_{R500} obtained from N_2 adsorption-desorption isotherms (Calcined at 550°C, reduced at 500°C for 2 hours, reaction temperature at 350°C, regeneration temperature at 350-500°C and space velocity was 22 L/(g h)).

Sample	**BET surface area [m^2/g]**
RMC_{R500}	31
RMC_{R500}, spent	24

In table 4.2.4 it is observed that the BET surface area of RMC_{R500} has decreased after the reaction. This is expected due to the adsorption reaction.

CHAPTER

FIVE

CONCLUSIONS

For this thesis, the Fe-based sorbent, red mud, has been synthesized, characterized and tested for gas dechlorination of a model system with chlorobenzene. The effect of washing and regeneration has been studied. Specifically, the effect of washing was studied by washing red mud with water and HCl. Red mud was characterized with XRD, XRF, TPR and N_2 adsorption-desorption isotherms. Finally, the activity for the various treatments of red mud was evaluated under the dechlorination reaction with different experimental conditions. Preparation of $FeCl_3/SiO_2$ was done to determine the experimental conditions for regeneration through characterization using XRF and TGA. Characterization and experiments with Fe/SiO_2 were also carried out to use as a reference.

Calcination of red mud at 550°C, increased the surface area to 24.3 m^2/g, while simultaneously eliminating components such as FeOOH, $Al(OH)_3$, and SiO_2. In comparison to Fe/SiO_2 which has a surface area of 451 m^2/g, the surface area of red mud remains relatively low. From the XRD and XRF analysis, it was observed that water did not have any significant impact on the composition and phases as they remained consistent after the treatment. After washing with HCl, cancrinite was completely removed and there was a significant improvement in the reduction of various components. The sodium content decreased by 97%, aluminum by 52%, silica by 80%, and calcium by 44%. In addition, the surface area was increased to 42 m^2/g. TPR analysis of RMC indicates that other elements in red mud are reducible as well. RMC shows a peak at about 400°C and 650°, indicating maximum hydrogen consumption.

It appears from the XRD results that RMC_{R350} and RMC_{500} contain a mixture of Fe_3O_4 and Fe^0. The TPR results show that RMC_{R350} achieve a higher reduction degree. This can be explained due to oxidation with time despite passivation, and a higher degree of Fe^0 in RMC_{R500}, which easier oxidizes. The oxidation with time can also explain the low difference in activity observed between RMC and RMC_{500} when reduced in-situ at 350°C prior to the reduction. In addition to that, red mud might not be sensitive to the reduction of iron and it could be other elements that contribute to the dechlorination reaction. The TPR results for RMC_{HCl} indicate that there are species that are not reducible below 900°C, and explain the negotiable difference in activity between RMC and RMC_{HCl}.

Due to the TGA analysis of $FeCl_3/SiO_2$ and an industrial point of view, a regeneration temperature at 350°C was chosen. Experiments with 500°C were carried out as a reference. Regeneration of Fe/SiO_2 at a temperature range of 350-450°C was found to be ineffective under the circumstances. For RMC, it was observed a negotiable difference in activity after regenerating at 350°C and 500°C. Furthermore, regenerating with RMC and RMC_{HCl} at 350°C also shows a negotiable difference in activity, indicating that washing with HCl was inefficient for regeneration under these circumstances. During the regeneration of RMC and RMC_{HCl}, it was observed that the activity shows varied behavior in activity. This behavior could be due to other elements in red mud contributing to the dechlorination reaction and the nonhomogenous character in addition to a mechanism that suggests that Fe_2O_3 initially acts as a catalyst and produces HCl. Contact between carbon, titanium and HCl can lead to the observed reactivity. In addition, a regeneration time of 1 hour could be inefficient according to TGA analysis.

It was discovered from the experiments that it was a challenge with the reproducibility of red mud. This could be due to the complex composition of red mud and the nonhomogenous character. Despite the challenges of reproducibility with red mud, it has been observed that red mud has a greater regeneration capability compared to Fe/SiO_2. This can be due to other elements in red mud contributing to the dechlorination reaction. From XRF after the reduction, it is observed that the chlorine has been adsorbed to its maximum capacity and XRD analysis displays that it is not a significant change in composition after the reaction.

To ensure reproducibility and the influence of reduction, it's important to examine the homogeneity of red mud due to its complex elemental composition that may pose these issues. Although there are challenges with reproducibility, it is worth investigating the regeneration ability due to the observed reactivity and relatively high activity compared to Fe/SiO_2. Furthermore, taking a closer look at red mud is worthwhile due to its high concentration of ferric oxide and low cost as a by-product, making it a potential candidate for dechlorination in plastic pyrolysis.

CHAPTER

SIX

FUTURE WORK

In order to explore the dechlorination with red mud it is important to discover the challenges with reproducibility. It could be interesting to utilize UV-vis and chemisorption to gain a deeper understanding of the dispersion of red mud. In addition, it is important to determine the possible active phases of other elements in red mud and the sensitivity for reduction. Specifically, the role of titanium, which was not studied in this thesis and could potentially aid in the dechlorination process due to its strong interaction with chlorine and metal. The sensitivity for reduction can be discovered with further characterization and experiments of other elements in red mud.

In addition, it is important to explore the dechlorination reaction and its mechanism. Currently, it is unclear whether $FeCl_2$ or $FeCl_3$ is formed during the process, making it important to determine the exact phase of iron chloride to understand the dechlorination mechanism for this model system. The use of spectroscopy, specifically IR, can be helpful in identifying the specific phases of iron chloride present.

It appears that red mud has decent regenerative abilities, but more research is needed to address the observed possible deactivation issue. Moreover, the TGA results suggest that the regeneration process may require additional time, and further investigation is needed to determine the exact duration and detect if this will lead to full chlorine regeneration. The potential observed reactivity could be linked to the formation of HCl gas. Detecting the presence of HCl and analyzing its mechanisms towards the sorbent might be necessary.

REFERENCES

[1] Yujie Peng et al. *A review on catalytic pyrolysis of plastic wastes to high-value products*. Feb. 2022. DOI: 10.1016/j.enconman.2022.115243.

[2] Roland Geyer, Jenna R Jambeck, and Kara Lavender Law. *Production, use, and fate of all plastics ever made*. Tech. rep. 2017. URL: https://www.science.org.

[3] David G. Bucknall. "Plastics as a materials system in a circular economy: Plastics in the Circular Economy". In: *Philosophical Transactions of the Royal Society A: Mathematical, Physical and Engineering Sciences*. Vol. 378. 2176. Royal Society Publishing, July 2020. DOI: 10.1098/rsta.2019.0268.

[4] *Thermosets, Thermoplastics, and the Environment*. URL: https://www.tencom.com/blog/thermosets-thermoplastics-and-the-environment.

[5] R. Miandad et al. "Plastic waste to liquid oil through catalytic pyrolysis using natural and synthetic zeolite catalysts". In: *Waste Management* 69 (Nov. 2017), pp. 66–78. ISSN: 0956-053X. DOI: 10.1016/J.WASMAN.2017.08.032.

[6] Yi Bo Zhao, Xu Dong Lv, and Hong Gang Ni. "Solvent-based separation and recycling of waste plastics: A review". In: *Chemosphere* 209 (Oct. 2018), pp. 707–720. ISSN: 0045-6535. DOI: 10.1016/J.CHEMOSPHERE.2018.06.095.

[7] *Plastic leakage and greenhouse gas emissions are increasing - OECD*. URL: https://www.oecd.org/environment/plastics/increased-plastic-leakage-and-greenhouse-gas-emissions.htm.

[8] Tobias D. Nielsen et al. "Politics and the plastic crisis: A review throughout the plastic life cycle". In: *Wiley Interdisciplinary Reviews: Energy and Environment* 9.1 (Jan. 2020), e360. ISSN: 2041-840X. DOI: 10.1002/WENE.360. URL: https://onlinelibrary.wiley.com/doi/full/10.1002/wene.360%20https://onlinelibrary.wiley.com/doi/abs/10.1002/wene.360%20https://wires.onlinelibrary.wiley.com/doi/10.1002/wene.360.

[9] Voulvoulis N et al. "Examining material evidence, the carbon footprint". In: *Imperial College London* (2019).

[10] European Commission. "plastics-strategy". In: *A European strategy for plastics in a circular economy* COM(2018) 28 final (2018).

[11] Ellen Palm et al. "Narrating plastics governance: policy narratives in the European plastics strategy". In: *Environmental Politics* 31.3 (2022), pp. 365–385. ISSN: 17438934. DOI: 10.1080/09644016.2021.1915020.

[12] *Historic day in the campaign to beat plastic pollution: Nations commit to develop a legally binding agreement*. URL: https://www.unep.org/news-and-stories/press-release/historic-day-campaign-beat-plastic-pollution-nations-commit-develop.

[13] Global Plastics Outlook: Policy Scenarios to 2060 OECD (2022). *Global Plastics Outlook: Policy Scenarios to 2060 | en | OECD*. DOI: https://doi.org/10.1787/aa1edf33-en.. URL: https://www.oecd.org/publications/global-plastics-outlook-aa1edf33-en.htm.

[14] Lesli O. Mark, Melissa C. Cendejas, and Ive Hermans. *The Use of Heterogeneous Catalysis in the Chemical Valorization of Plastic Waste*. Nov. 2020. DOI: 10.1002/cssc.202001905.

[15] *How Is Plastic Made? A Simple Step-By-Step Explanation*. URL: https://www.bpf.co.uk/plastipedia/how-is-plastic-made.aspx.

[16] Zoé O.G. Schyns and Michael P. Shaver. *Mechanical Recycling of Packaging Plastics: A Review*. Feb. 2021. DOI: 10.1002/marc.202000415.

[17] Laurens Delva et al. *AN INTRODUCTORY REVIEW MECHANICAL RECYCLING OF POLYMERS FOR DUMMIES*. Tech. rep.

[18] Salma Belbessai, Abir Azara, and Nicolas Abatzoglou. *Recent Advances in the Decontamination and Upgrading of Waste Plastic Pyrolysis Products: An Overview*. Apr. 2022. DOI: 10.3390/pr10040733.

[19] Shafferina Dayana Anuar Sharuddin et al. "A review on pyrolysis of plastic wastes". In: *Energy Conversion and Management* 115 (May 2016), pp. 308–326. ISSN: 0196-8904. DOI: 10.1016/J.ENCONMAN.2016.02.037.

[20] Irdanto Saputra Lase et al. "How much can chemical recycling contribute to plastic waste recycling in Europe? An assessment using material flow analysis modeling". In: *Resources, Conservation and Recycling* 192 (May 2023), p. 106916. ISSN: 0921-3449. DOI: 10.1016/J.RESCONREC.2023.106916.

[21] Harish Jeswani et al. "Life cycle environmental impacts of chemical recycling via pyrolysis of mixed plastic waste in comparison with mechanical recycling and energy recovery". In: *Science of The Total Environment* 769 (May 2021), p. 144483. ISSN: 0048-9697. DOI: 10.1016/J.SCITOTENV.2020.144483.

[22] *Recycling and the future of the plastics industry | McKinsey*. URL: https://www.mckinsey.com/industries/chemicals/our-insights/how-plastics-waste-recycling-could-transform-the-chemical-industry#/.

[23] Muhammad Saad Qureshi et al. "Pyrolysis of plastic waste: Opportunities and challenges". In: *Journal of Analytical and Applied Pyrolysis* 152 (Nov. 2020), p. 104804. ISSN: 0165-2370. DOI: 10.1016/J.JAAP.2020.104804.

[24] Marvin Kusenberg et al. "Opportunities and challenges for the application of post-consumer plastic waste pyrolysis oils as steam cracker feedstocks: To decontaminate or not to decontaminate?" In: *Waste Management* 138 (Feb. 2022), pp. 83–115. ISSN: 0956-053X. DOI: 10.1016/J.WASMAN.2021.11.009.

[25] R. Miandad et al. "Catalytic pyrolysis of plastic waste: A review". In: *Process Safety and Environmental Protection* 102 (July 2016), pp. 822–838. ISSN: 0957-5820. DOI: 10.1016/J.PSEP.2016.06.022.

[26] Mehdi Sadat-Shojai and Gholam Reza Bakhshandeh. "Recycling of PVC wastes". In: *Polymer Degradation and Stability* 96.4 (Apr. 2011), pp. 404–415. ISSN: 0141-3910. DOI: 10.1016/J.POLYMDEGRADSTAB.2010.12.001.

[27] N. Lingaiah et al. "Catalytic dechlorination of chloroorganic compounds from PVC-containing mixed plastic-derived oil". In: *Applied Catalysis A: General* 207.1-2 (Feb. 2001), pp. 79–84. ISSN: 0926-860X. DOI: 10.1016/S0926-860X(00)00656-6.

[28] Jan Hubáček et al. "Dechlorination during pyrolysis of plastics: The potential of stepwise pyrolysis in combination with metal sorbents". In: *Fuel Processing Technology* 231 (June 2022), p. 107226. ISSN: 0378-3820. DOI: 10.1016/J.FUPROC.2022.107226.

[29] A. Lopez-Urionabarrenechea et al. "Catalytic stepwise pyrolysis of packaging plastic waste". In: *Journal of Analytical and Applied Pyrolysis* 96 (July 2012), pp. 54–62. ISSN: 0165-2370. DOI: 10.1016/J.JAAP.2012.03.004.

[30] *Catalytic metals and their uses | The Mole | RSC Education*. URL: https://edu.rsc.org/feature/catalytic-metals-and-their-uses/3007558.article#commentsJump.

[31] M. A. Khairul, Jafar Zanganeh, and Behdad Moghtaderi. "The composition, recycling and utilisation of Bayer red mud". In: *Resources, Conservation and Recycling* 141 (Feb. 2019), pp. 483–498. ISSN: 0921-3449. DOI: 10.1016/J.RESCONREC.2018.11.006.

[32] *Red mud, et unødvendig problem? - #SINTEFblogg*. URL: https://blogg.sintef.no/industri/red-mud-unodvendig-problem/.

[33] Rosa Miranda et al. "Vacuum pyrolysis of PVC I. Kinetic study". In: *Polymer Degradation and Stability* 64.1 (Apr. 1999), pp. 127–144. ISSN: 0141-3910. DOI: 10.1016/S0141-3910(98)00186-4.

[34] R. Miandad et al. "Effect of plastic waste types on pyrolysis liquid oil". In: *International Biodeterioration & Biodegradation* 119 (Apr. 2017), pp. 239–252. ISSN: 0964-8305. DOI: 10.1016/J.IBIOD.2016.09.017.

[35] A. López et al. "Catalytic pyrolysis of plastic wastes with two different types of catalysts: ZSM-5 zeolite and Red Mud". In: *Applied Catalysis B: Environmental* 104.3-4 (May 2011), pp. 211–219. ISSN: 0926-3373. DOI: 10.1016/J.APCATB.2011.03.030.

[36] Marina A. Ermakova et al. "Decomposition of methane over iron catalysts at the range of moderate temperatures: The influence of structure of the catalytic systems and the reaction conditions on the yield of carbon and morphology of carbon filaments". In: *Journal of Catalysis* 201.2 (2001), pp. 183–197. ISSN: 00219517. DOI: 10.1006/jcat.2001.3243.

[37] Guozhan Jiang et al. "Understanding the Dechlorination of Chlorinated Hydrocarbons in the Pyrolysis of Mixed Plastics". In: *ACS Sustainable Chemistry and Engineering* 9.4 (Feb. 2021), pp. 1576–1589. ISSN: 21680485. DOI: 10.1021/ACSSUSCHEMENG.0C06461/SUPPL{_}FILE/SC0C06461{_}SI{_}001.PDF. URL: https://pubs.acs.org/doi/abs/10.1021/acssuschemeng.0c06461.

[38] Yong-Xi Li, Hui Li, and Kenneth J Klabunde. *Destructive Adsorption of Chlorinated Benzenes on Ultrafine (Nanoscale) Particles of Magnesium Oxide and Calcium Oxide*. Tech. rep. 1994, pp. 1248–1253. URL: https://pubs.acs.org/sharingguidelines.

[39] C F Cullis and J E Manton. *THE PYROLYSIS OF CHLOROBENZENE*. Tech. rep. 1958.

[40] A. López et al. "Dechlorination of fuels in pyrolysis of PVC containing plastic wastes". In: *Fuel Processing Technology* 92.2 (Feb. 2011), pp. 253–260. ISSN: 0378-3820. DOI: 10.1016/J.FUPROC.2010.05.008.

[41] Jan Snow et al. "Dechlorination during pyrolysis of plastics: Effect of municipal plastic waste composition". In: *Fuel Processing Technology* 248 (Sept. 2023), p. 107823. ISSN: 0378-3820. DOI: 10.1016/J.FUPROC.2023.107823. URL: https://linkinghub.elsevier.com/retrieve/pii/S0378382023001716.

[42] N. Lingaiah et al. "Catalytic dechlorination of chloroorganic compounds from PVC-containing mixed plastic-derived oil". In: *Applied Catalysis A: General* 207.1-2 (Feb. 2001), pp. 79–84. ISSN: 0926-860X. DOI: 10.1016/S0926-860X(00)00656-6.

[43] Qi Wang et al. "Calcination temperature induced structural change of red mud and its enhanced catalytic performance for hydrocarbon-based biofuels production". In: *Fuel Processing Technology* 233 (Aug. 2022), p. 107316. ISSN: 03783820. DOI: 10.1016/j.fuproc.2022.107316. URL: https://linkinghub.elsevier.com/retrieve/pii/S0378382022001564.

[44] S. Ordóñez, H. Sastre, and F. V. Díez. "Characterisation and deactivation studies of sulfided red mud used as catalyst for the hydrodechlorination of tetrachloroethylene". In: *Applied Catalysis B: Environmental* 29.4 (Feb. 2001), pp. 263–273. ISSN: 0926-3373. DOI: 10.1016/S0926-3373(00)00207-1.

[45] Kerry C. Pratt and Victor Christoverson. "Hydrogenation of a model hydrogen-donor system using activated red mud catalyst". In: *Fuel* 61.5 (May 1982), pp. 460–462. ISSN: 0016-2361. DOI: 10.1016/0016-2361(82)90072-2.

[46] J. R. Paredes et al. "Catalytic combustion of methane over red mud-based catalysts". In: *Applied Catalysis B: Environmental* 47.1 (Jan. 2004), pp. 37–45. ISSN: 09263373. DOI: 10.1016/S0926-3373(03)00325-4.

[47] H. Soner Altundoan et al. "Arsenic adsorption from aqueous solutions by activated red mud". In: *Waste Management* 22.3 (June 2002), pp. 357–363. ISSN: 0956-053X. DOI: 10.1016/S0956-053X(01)00041-1.

[48] Snigdha Sushil and Vidya S. Batra. "Catalytic applications of red mud, an aluminium industry waste: A review". In: *Applied Catalysis B: Environmental* 81.1-2 (May 2008), pp. 64–77. ISSN: 0926-3373. DOI: 10.1016/J.APCATB.2007.12.002.

[49] Bahareh A.T. Mehrabadi et al. "A Review of Preparation Methods for Supported Metal Catalysts". In: *Advances in Catalysis*. Vol. 61. Academic Press Inc., 2017, pp. 1–35. DOI: 10.1016/bs.acat.2017.10.001.

[50] *How Calcination is Used in Catalyst Preparation*. URL: https://feeco.com/how-calcination-is-used-in-catalyst-preparation/.

[51] Simo Olavi Pehkonen and Shaojun Yuan. "Self-Assembly Ultrathin Film Coatings for the Mitigation of Corrosion: General Considerations". In: *Interface Science and Technology* 23 (Jan. 2018), pp. 13–21. ISSN: 1573-4285. DOI: 10.1016/B978-0-12-813584-6.00002-8.

[52] M. A. Reiche, M. Maciejewski, and A. Baiker. "Characterization by temperature programmed reduction". In: *Catalysis Today* 56.4 (Mar. 2000), pp. 347–355. ISSN: 0920-5861. DOI: 10.1016/S0920-5861(99)00294-1.

[53] *X-ray diffraction (XRD) :: Anton Paar Wiki*. URL: https://wiki.anton-paar.com/se-en/x-ray-diffraction-xrd/.

[54] *What is XRF (X-ray fluorescence) and How Does it Work?* URL: https://www.thermofisher.com/blog/ask-a-scientist/what-is-xrf-x-ray-fluorescence-and-how-does-it-work/.

[55] *XRF: X-Ray Fluorescence Spectroscopy | Hi Rel Parts | Alter Technology*. URL: https://wpo-altertechnology.com/xrf-x-ray-fluorescence-spectroscopy-hi-rel-parts/.

[56] Nooshin Saadatkhah et al. "Experimental methods in chemical engineering: Thermogravimetric analysis—TGA". In: *The Canadian Journal of Chemical Engineering* 98.1 (Jan. 2020), pp. 34–43. ISSN: 1939-019X. DOI: 10.1002/CJCE.23673. URL: https://onlinelibrary.wiley.com/doi/full/10.1002/cjce.23673%20https://onlinelibrary.wiley.com/doi/abs/10.1002/cjce.23673%20https://onlinelibrary.wiley.com/doi/10.1002/cjce.23673.

[57] Kenneth S.W. Sing. "Adsorption methods for the characterization of porous materials". In: *Advances in Colloid and Interface Science* 76-77 (July 1998), pp. 3–11. ISSN: 0001-8686. DOI: 10.1016/S0001-8686(98)00038-4.

[58] Raoof Bardestani, Gregory S. Patience, and Serge Kaliaguine. *Experimental methods in chemical engineering: specific surface area and pore size distribution measurements—BET, BJH, and DFT*. Nov. 2019. DOI: 10.1002/cjce.23632.

[59] Prof. De Chen. *Personal contact*. Trondheim, May 2023.

APPENDICES

A - CALCULATIONS

.1 Sorbent calculations

.1.1 Data

Table .1.1 displays the data utilized for the calculation for preparation of Fe/SiO_2 and $FeCl_3/SiO_2$.

Table .1.1: Data utilized for preparation of $FeSiO_2$ and $FeCl_3/SiO_2$

Variable/constant	**Value**	**Unit**
Solubility of iron nitrate	825	g/l
V_{pore} of SiO_2	0.9	mL/g
Total volume	10	mL
Purity of iron nitrate	98	%
Molecular weight of Fe_2O_3	159.7	g/mol
Molecular weight of iron nitrate nonahydrate	404	g/mol
Molecular weight of iron	55.8	g/mol

.1.2 Sorbent preparation

For the preparation of Fe/SiO_2, the quantity of SiO_2 needs to be calculated. The calculation of the SiO_2 quantity is conducted as follows:

$$\frac{10 \text{ mL}}{0.9 \text{ mL/g}} = 11.11 \text{ g } SiO_2 \tag{1}$$

Assuming that the solubility of iron nitrate is 0.8 g/mL. The amount of iron nitrate required is calculated as follows:

$$10 \text{ mL} \cdot \frac{0.8 \text{ g iron nitrate}}{1 \text{ mL}} \frac{1}{0.98} = 8.16 \text{ g iron nitrate} \tag{2}$$

Further, the amount of iron can be determined as follows:

$$8.16 \text{ g iron nitrate} \frac{1 \text{ mol Fe}}{404 \text{ g iron nitrate}} \frac{55.8 \text{ g Fe}}{1 \text{ mol Fe}} = 1.105 \text{ g Fe} \tag{3}$$

To calculate the percentage of Fe present in $FeSiO_2$, it is necessary to calculate the amount of Fe_2O_3. This calculation is as follows:

$$\frac{1.105 \text{ g Fe}}{55.8 \text{ g Fe/mol}} \frac{1 \text{ mol } Fe_2O_3}{2 \text{ mol Fe}} \frac{159.69 \text{ g } Fe_2O_3}{1 \text{ mol } Fe_2O_3} = 1.58 \text{ g } Fe_2O_3 \tag{4}$$

The percentage of iron in $FeSiO_2$ is calcualted as follows:

$$\% \text{ Fe} = \frac{m_{Fe}}{m_{Fe2O3} + m_{SiO2}} = \frac{1.105 \text{ g}}{1.58 \text{ g} + 11.11 \text{ g}} \cdot 100 = 8.7\% \tag{5}$$

The percentage of Fe_2O_3 in $FeSiO_2$ is calculated as follow:

$$\% \text{ } Fe_2O_3 = \frac{m_{Fe2O3}}{m_{Fe2O3} + m_{SiO2}} = \frac{1.58 \text{ g}}{1.58 \text{ g} + 11.11 \text{ g}} \cdot 100 = 12.45\% \tag{6}$$

Furthermore, the amount of $FeCl_3$ was calculated as follows:

$$0.1245 \cdot (\text{m}FeCl_3 + \text{m}SiO_2 = 0.1245 \cdot (\text{m}FeCl_3 + 1.383 = \text{m}FeCl_3 \tag{7}$$

Which further gives:

$$\frac{1.383g}{1 - 0.1245} = 1.58g \tag{8}$$

Due to 97% purity, this gives a mass of 1.63 g of $FeCl_3$.

.1.3 Hydrogen uptake

The theoretical value for hydrogen consumption for Fe/SiO_2 can be determined from stoichiometry from 2.1, 2.2 and 2.4. The theoretical values are calculated per gram sorbent. As already calculated, the content of Fe_2O_3 is 12.45%. The amount of moles hydrogen required to reduce Fe_2O_3 is calculated as follows:

$$0.124 \text{ g } Fe_2O_3 \cdot \frac{1 \text{ mol } Fe_2O_3}{159.7 \text{ g } Fe_2O_3} \frac{1 \text{ mol } H_2}{3 \text{ mol } Fe_2O_3} \cdot 10^6 = 258\mu\text{mol } H_2\text{/g sorbent} \tag{9}$$

The amount of moles of hydrogen required to reduce Fe_3O_4 is calculated based on stoichiometry in equation 2.2, as follows:

$$0.124 \text{ g } Fe_2O_3 \frac{1 \text{ mol } Fe_2O_3}{159.7 \text{ g } Fe_2O_3} \frac{2 \text{ mol } Fe_3O_4}{3 \text{ mol } Fe_2O_3} \frac{1 \text{ mol } H_2}{1 \text{ mol } Fe_3O_4} \cdot 10^6 = 518\mu\text{mol } H_2\text{/g sorbent} \tag{10}$$

The amount of moles hydrogen required to reduce FeO is calculated based on stoichiometry in equation 2.3, as follows:

$$0.124 \text{ g } Fe_2O_3 \frac{1 \text{ mol } Fe_2O_3}{159.7 \text{ g } Fe_2O_3} \frac{2 \text{ mol } Fe_3O_4}{3 \text{ mol } Fe_2O_3} \frac{3 \text{ mol FeO}}{1 \text{ mol } Fe_3O_4} \frac{1 \text{ mol } H_2}{1 \text{ mol FeO}} \cdot 10^6 = 1553\mu\text{mol } H_2\text{/g sorbent} \tag{11}$$

The theoretical values of hydrogen consumption of red mud were calculated from the same stoichiometry. The amount of Fe_2O_3 was based on the values from XRF analysis.

.2 Conversion and capacity of sorbents

.2.1 Data

Table .2.1 displays the data utilized for the calculation of chlorobenzene conversion and capacity for the dechlorination reaction.

Table .2.1: Data utilized for the calculation of chlorobenzene conversion and capacity for the dechlorination reaction.

Variable/constant	Value	Unit
Total flow	110	mL/min
CB in flow	0.005	%
Pressure	1	atm
Gas constant	0.082	L atm/K mol
Temperature	273	K
Molecular weight of CB	112.56	g/mol
Molecular weight of Cl	35.43	g/mol

.2.2 Calculations

The conversion, x, of chlorobenzene, is calculated from the ratio of nitrogen to chlorobenzene areas, obtained from the GC. The calculation is as follows:

$$\frac{\frac{\text{Feed CB area}}{\text{Feed } N_2 \text{ area}} - \frac{\text{CB area}}{N_2 \text{ area}}}{\frac{\text{Feed CB area}}{\text{Feed } N_2 \text{ area}}} \cdot 100 = x \tag{12}$$

Furthermore, the capacity could be calculated. By multiplying the total flow rate of 110 mL/min with 0.000005, the amount of CB in the flow can be determined to be 0.0055 mL/min. The quantity of chlorobenzene in the outlet is calculated as follows:

$$0.0055 \text{ mL/min - } (0.0055 \text{ mL/min} \cdot \text{x}) = \text{CB mL/min in the outlet} \tag{13}$$

To determine the amount of chlorobenzene reacted per gram of catalyst, one can analyze the summary of the area under the curve of mL of chlorobenzene per minute reacted versus time. The mmol chlorobenzene reacted/g catalyst are calculated by multiplying with the ideal gas law, as follows:

$$\frac{\text{mL CB react} \cdot \text{p}}{\text{nRT} \cdot \text{g sorbent}} = \frac{\text{mL CB react}}{22.4 \cdot \text{g sorbent}} = \text{mmol CB/g sorbent} \tag{14}$$

The capacity, calculated from the chlorobenzene reacted, can be determined as follows:

$$\text{mmol CB/g sorbent} \cdot 112.56 \text{ g CB/mol} = \text{mg CB react/g sorbent} \tag{15}$$

The capacity, calculated from the chlorine adsorbed, can be determined with stoichiometry as follows:

$$\frac{\text{mg CB}}{\text{g sorbent}} \frac{\text{mol CB}}{112.56 \text{ g CB}} \frac{1 \text{ mol CB}}{1 \text{ mol Cl}} \frac{35.43\text{g Cl}}{1 \text{ mol Cl}} = \text{mg Cl adsorbed/g sorbent} \tag{16}$$

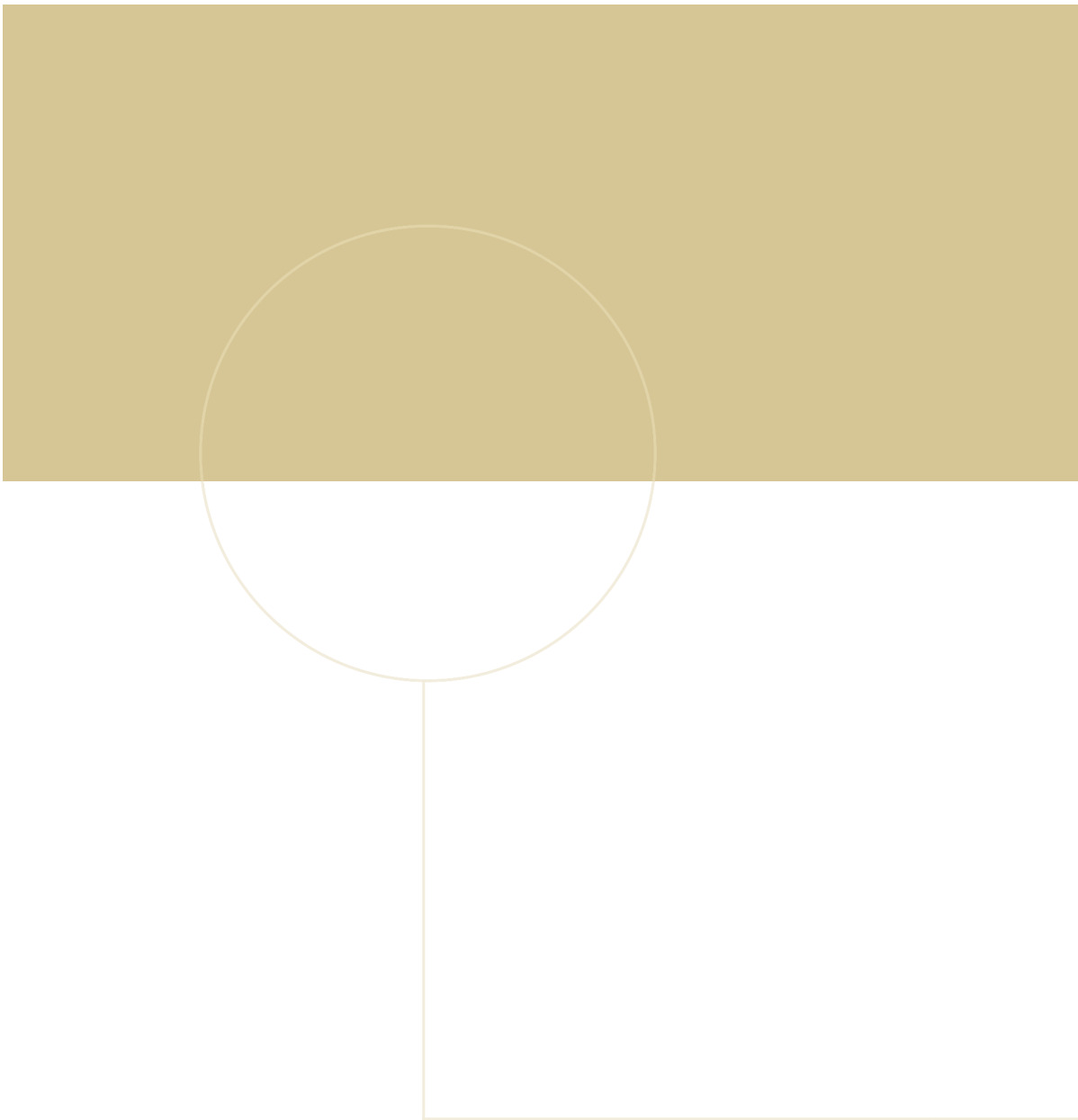

NTNU

Norwegian University of
Science and Technology